

Observational constraints on the sub-galactic matter-power spectrum from galaxy-galaxy strong gravitational lensing

D. Bayer,^{1*} S. Chatterjee,¹ L. V. E. Koopmans,¹ S. Vegetti,² J. P. McKean,^{1,3} T. Treu,⁴ and C. D. Fassnacht⁵

¹*Kapteyn Astronomical Institute, University of Groningen, PO Box 800, 9700 AV Groningen, the Netherlands*

²*Max Planck Institute for Astrophysics, Karl-Schwarzschild-Strasse 1, D-85740 Garching, Germany*

³*ASTRON, Netherlands Institute for Radio Astronomy, Postbus 2, NL-7990 AA, Dwingeloo, the Netherlands*

⁴*Department of Physics and Astronomy, UCLA, 430 Portola Plaza, Los Angeles, CA 90095-1547, USA*

⁵*Department of Physics, University of California, Davis, 1 Shields Ave. Davis, CA 95616, USA*

submitted to MNRAS

ABSTRACT

Constraining the sub-galactic matter-power spectrum on 1-10 kpc scales would make it possible to distinguish between the concordance Λ CDM model and various alternative dark-matter models due to the significantly different levels of predicted mass structure. Here, we demonstrate a novel approach to observationally constrain the population of overall low-mass density fluctuations in the inner regions of massive elliptical lens galaxies, based on the power spectrum of the associated surface-brightness perturbations observable in highly magnified galaxy-scale Einstein rings and gravitational arcs. The application of our method to the SLACS lens system SDSS J0252+0039 results in the following limits (at the 99 per cent confidence level) on the dimensionless convergence-power spectrum (and the associated standard deviation in aperture mass): $\Delta_{\delta\kappa}^2 < 1$ ($\sigma_{AM} < 0.8 \times 10^8 M_{\odot}$) on 0.5-kpc scale, $\Delta_{\delta\kappa}^2 < 0.1$ ($\sigma_{AM} < 1 \times 10^8 M_{\odot}$) on 1-kpc scale and $\Delta_{\delta\kappa}^2 < 0.01$ ($\sigma_{AM} < 3 \times 10^8 M_{\odot}$) on 3-kpc scale. The estimated effect of CDM sub-haloes lies considerably below these first observational upper-limit constraints on the level of inhomogeneities in the projected total mass distribution of galactic haloes. Future analysis for a larger sample of galaxy-galaxy strong lens systems will narrow down these constraints and rule out all cosmological models predicting a significantly larger level of clumpiness on these critical sub-galactic scales.

Key words: cosmology: observations – dark matter – galaxies: individual: SDSS J0252+0039 – galaxies: structure – gravitational lensing: strong – methods: statistical

1 INTRODUCTION

The dark energy plus cold dark matter (Λ CDM) concordance cosmological model successfully reproduces the observed large-scale (larger than ~ 1 Mpc) distribution of matter in the Universe (e.g. Vogelsberger et al. 2014; Schaye et al. 2015; Planck Collaboration et al. 2016; Guo et al. 2016). However, on smaller galactic and sub-galactic scales, theory and observations appear to diverge (see Bullock & Boylan-Kolchin 2017, for a recent review on the small-scale challenges to the Λ CDM paradigm). One of the main discrepancies, known as the Missing Satellites Problem (MSP), lies in the fact that the number of dwarf satellite galaxies observed in the Local Group (~ 100 , e.g. McConnachie 2012; Drlica-Wagner et al. 2015) is much lower than the numerous abundance of substructure populating galactic haloes in Λ CDM-based numerical simulations of cosmological structure formation (e.g. Klypin et al. 1999; Moore

et al. 1999; Diemand et al. 2007; Nierenberg et al. 2016; Dooley et al. 2017).

The currently favoured interpretation of the MSP states that the missing predicted sub-haloes do exist, but are extremely inefficient at forming stars due to a variety of baryonic processes (such as feedback from massive stars and active galactic nuclei, tidal stripping, heating of intergalactic gas by the ultraviolet photo-ionising background or photo-ionization squelching, e.g. Thoul & Weinberg 1996; Bullock et al. 2000; Somerville 2002; Sawala et al. 2014; Despali et al. 2017; Kim et al. 2017), and thus remain undetectable for conventional imaging surveys. Alternatively, the discrepancy might point towards dark-matter models with larger thermal velocities at early times, leading to an increased free-streaming length below which structure formation is suppressed (referred to as warm dark matter or WDM, Bode et al. 2001), see e.g. Menci et al. (2012), Nierenberg et al. (2013), Viel et al. (2013), Lovell et al. (2014) and Vegetti et al. (2018) for some recent studies. Lastly, the Local Group might just be a biased environment with less abundant substructure,

* Contact e-mail: bayer@astro.rug.nl

not representative of the entire Universe (e.g. [Muller et al. 2018](#)). Therefore, in order to fully clarify the above ambiguities and test the mentioned solutions to the small-scale problems of the Λ CDM paradigm, it is crucial to study mass structure in galaxies beyond the Local Universe. In particular, constraining the matter-clustering properties on the critical sub-galactic 1-10 kpc scales would make it possible to distinguish between both various galaxy-formation scenarios within the Λ CDM model and the alternative dark-matter models (such as WDM), due to the considerably different levels of predicted mass structure.

The key techniques allowing to detect and quantify both faint and truly dark mass concentrations in galaxies at cosmological distances are based on an indirect study of their gravitational imprints on the lensed images in galaxy-scale strong gravitational lens systems, e.g. in the form of flux-ratio anomalies observed in multiply imaged gravitationally lensed quasars (e.g. [Mao & Schneider 1998](#); [Metcalf & Madau 2001](#); [Dalal & Kochanek 2002](#); [Nierenberg et al. 2014](#); [Gilman et al. 2017a](#)) or surface-brightness perturbations arising in the extended lensed emission of a background-source galaxy (e.g. [Koopmans 2005](#); [Vegetti & Koopmans 2009a](#); [Vegetti et al. 2010a,b](#)) – investigated in this work.

Due to the phenomenon of galaxy-galaxy strong gravitational lensing, light rays originating from the background-source galaxy are gravitationally deflected while passing by the gravitational field of the foreground lens galaxy on their way towards the observer. This gravitational deflection transforms the observed surface-brightness distribution of the background galaxy and leads to the appearance of lensed images (such as multiple images, gravitational arcs or a complete Einstein ring). Besides the geometrical configuration of the lens system and the original background-source light emission, the observed surface-brightness distribution of the lensed images is crucially determined by the distribution of the total (dark-matter and baryonic) lensing mass, for simplicity commonly assumed to be smooth in the lens-modelling procedure. Density inhomogeneities, if present in the lens galaxy or along its line-of-sight, result in perturbations to this otherwise smoothly-distributed lensing mass and, thus, slightly modify the resulting observed surface-brightness distribution of the lensed background source with respect to the smooth-lens model. The resulting observable surface-brightness anomalies in the lensed images can be modelled and traced back to the underlying density fluctuations in the lensing mass distribution, allowing one to infer the existence and quantify properties of mass structure in the foreground lens galaxy. Based on this insight, [Koopmans \(2005\)](#) and [Vegetti & Koopmans \(2009a\)](#) developed the indirect *gravitational-imaging technique*, aiming at the detection of individual dark-matter sub-haloes in lens galaxies, and proved that galactic sub-haloes at cosmological distances can be successfully identified as localised corrections to the smooth gravitational potential ([Vegetti et al. 2010c, 2012](#)), with the detection threshold depending on the angular resolution of the available data. Recently, [Despali et al. \(2017\)](#) showed that this technique can also be used to detect individual line-of-sight haloes and [Vegetti et al. \(2018\)](#) derived the resulting constraints on the properties of dark matter.

In order to investigate smaller mass-density fluctuations possibly existing in galactic haloes below the detection threshold of the gravitational-imaging technique for individual sub-haloes, [Bus \(2012\)](#) and [Hezaveh et al. \(2016\)](#) independently proposed a complementary statistical method. Instead of single localised potential corrections representing individual galactic sub-haloes, as discussed by [Vegetti & Koopmans \(2009a\)](#), in this alternative approach, the entire population of low-mass structure in the foreground lens galaxy is constrained statistically, in terms of the projected substructure

power spectrum, based on the observable collectively-induced surface-brightness perturbations in the extended lensed emission of the background source galaxy.

Contrary to the considerable number of recent theoretical studies (e.g. [Hezaveh et al. 2016](#); [Diaz Rivero et al. 2018](#)), little research has been done so far to actually measure or place observational constraints on the substructure-power spectrum from galaxy-galaxy strong gravitational lensing. The biggest challenge in this respect is that, besides the possible CDM substructure in the halo of the lens galaxy or along its line-of-sight, in reality the observed surface-brightness anomalies can also arise from other fluctuations in the complex distribution of dark matter and baryonic mass in the lens galaxy, such as e.g. stellar streams or edge-on discs ([Vegetti et al. 2014](#); [Gilman et al. 2017b](#); [Hsueh et al. 2016, 2017a,b](#)), not explicitly included in the smooth-lens model. Instead of focusing on substructure only, a possible realistic way of approaching this problem is thus to infer observational constraints on the statistical properties of overall departures from the best-fitting smooth-lens model and compare the results with predictions from hydrodynamical simulations (such as Illustris or EAGLE, [Vogelsberger et al. 2014](#); [Schaye et al. 2015](#)), accounting for both dark matter and various baryonic processes.

Further developing this idea, [Chatterjee & Koopmans \(2018\)](#) suggested that the level of such density variations in the total (both dark and baryonic) projected mass distribution of a lens galaxy can be observationally constrained when treated as a statistical ensemble and modelled in terms of Gaussian-Random-Field (GRF) potential perturbations superposed on the best-fitting smoothly-varying lensing potential. Within the developed theoretical formalism (see [Chatterjee & Koopmans 2018](#)), both the GRF perturbations to the total lensing potential and the resulting observable surface-brightness anomalies in the lensed images are quantified in a statistical way – in terms of their power spectra – and related to each other. This relation makes it possible to infer observational constraints on the free parameters of the power-law power spectrum assumed to describe the GRF-potential perturbations (variance of the GRF fluctuations and the power-law slope) from the measured power spectrum of the observed surface-brightness anomalies in the lensed images.

After successful tests of this new approach on simulated mock perturbed lens systems with an a priori known smooth-lens model, presented by [Chatterjee & Koopmans \(2018\)](#), our current long-term goal is to constrain the level of such Gaussian potential perturbations in a sample of observed (massive elliptical) gravitational lens galaxies around redshift $z \sim 0.2$. We emphasize that, in reality, the investigated perturbations may arise from a variety of different inhomogeneities in the total projected mass density of the lens galaxy, such as e.g. globular clusters, tidal streams, distortions in the baryonic mass distribution, CDM density fluctuations or mass structure along the line-of-sight. In the course of our analysis, we do not distinguish between these different sources, but attempt to derive the first observational upper-limit constraints on the total projected matter-power spectrum in galaxies on the sub-galactic 1-10 kpc scales. In this work, we introduce the methodology allowing us to apply the new statistical approach to observational data and present the results from our analysis of the galaxy-galaxy strong gravitational lens system SDSS J0252+0039 from the Sloan Lens ACS Survey (SLACS, [Bolton et al. 2008](#)), at redshift $z \sim 0.28$, observed with the Wide Field Camera 3 (WFC3) on board the *Hubble Space Telescope* (HST) in the F390W-band. A comparison of these constraints with predictions from hydrodynamical simulations for the Λ CDM and alternative dark-matter models will be performed in our next paper.

The present paper is divided into four parts. Section 2 provides a concise description of the problem under consideration, the GRF-formalism applied to model the mass-density fluctuations in galactic haloes and our procedure adopted to uncover, quantify and interpret the resulting surface-brightness anomalies in the HST-imaging of the studied lens systems. In Section 3, the methodology is explained in more detail and applied to our pilot system SDSS J0252+0039 from the SLACS Survey, leading to the first observational constraints on the power spectrum of GRF-potential perturbations and the corresponding density fluctuations in a (massive elliptical) lens galaxy, presented in Section 4. The final Section 5 provides conclusions and implications of this work for further research.

Throughout the paper we assume the following cosmology: $H_0 = 73 \text{ km s}^{-1} \text{ Mpc}^{-1}$, $\Omega_M = 0.25$ and $\Omega_\Lambda = 0.75$. Given this cosmology, 1 arcsec corresponds to 4.11 kpc at the redshift of the studied lens galaxy ($z_L = 0.280$) and 7.88 kpc at the redshift of the source galaxy ($z_S = 0.982$).

2 METHODOLOGY

As stated in the introduction, the final goal of this research is to infer observational constraints on the sub-galactic matter-power spectrum based on observable surface-brightness anomalies in the lensed images of galaxy-galaxy strong gravitational lens systems. In this section, we present the main concepts and a concise overview of our methodology allowing us to reach this goal. We begin by discussing the origin of the surface-brightness anomalies in the lensed images as gravitational signatures of mass-density fluctuations in the foreground lens galaxy in Section 2.1. In Section 2.2, after summarising the formalism of GRF-potential perturbations introduced by Chatterjee & Koopmans (2018), we relate the hypothetical perturbations in the lensing potential to the corresponding perturbations in the lensing-mass distribution and the deflection-angle field. Section 2.3 outlines the procedure allowing us to uncover the possible surface-brightness anomalies in the lensed images of galaxy-scale lens systems, use them to study the statistical properties of the underlying Gaussian perturbations to the smooth lensing potential and, finally, infer constraints on the associated density fluctuations in the lensing-mass distribution. The outlined methodology is explained in more detail and applied to the galaxy-galaxy strong gravitational lens system SDSS J0252+0039 from the Sloan Lens ACS Survey in Section 3.

2.1 Surface-brightness anomalies in the lensed images

We consider a galaxy-galaxy strong gravitational lens system with the observed surface-brightness distribution of the lensed images $I(\mathbf{x})$ as a function of the position in the lens plane \mathbf{x} . Intrinsically, such a system is characterised by the (unknown) projected mass density $\Sigma(\mathbf{x})$ of the foreground lens galaxy, the (unknown) surface-brightness distribution of the background source $S(\mathbf{y})$ (as a function of the position in the source plane \mathbf{y}) and the (known) spatial configuration given by the angular diameter distances from the observer to the lens D_d , from the observer to the source D_s and from the lens to the source D_{ds} . Following the convention of strong gravitational lensing, we express the projected lensing-mass density $\Sigma(\mathbf{x})$ in units of the critical surface-mass density Σ_{cr} for the specific spatial configuration of the considered lens system:

$$\Sigma_{cr} = \frac{c^2}{4\pi G} \times \frac{D_s}{D_d D_{ds}} \quad (1)$$

to obtain the commonly used (dimensionless) convergence $\kappa(\mathbf{x})$:

$$\kappa(\mathbf{x}) = \Sigma(\mathbf{x}) / \Sigma_{cr} \quad (2)$$

and the lensing potential $\psi(\mathbf{x})$:

$$\psi(\mathbf{x}) = \frac{1}{\pi} \int \mathbf{d}\mathbf{x}' \kappa(\mathbf{x}') \ln |\mathbf{x} - \mathbf{x}'| \quad (3)$$

by solving the Poisson equation:

$$\nabla^2 \psi(\mathbf{x}) = 2 \times \kappa(\mathbf{x}). \quad (4)$$

The associated (scaled) deflection-angle field $\alpha(\mathbf{x})$:

$$\alpha(\mathbf{x}) = \nabla \psi(\mathbf{x}) \quad (5)$$

determines a mapping between the corresponding positions in the lens- and the source plane, encapsulated in the lens equation:

$$\mathbf{y}(\mathbf{x}) = \mathbf{x} - \alpha(\mathbf{x}) = \mathbf{x} - \nabla \psi(\mathbf{x}). \quad (6)$$

This mapping together with the principle of the surface-brightness conservation in strong gravitational lensing:

$$I(\mathbf{x}) = S(\mathbf{y}(\mathbf{x})) \quad (7)$$

builds the foundation for numerical grid-based smooth-lens modelling codes (e.g. the adaptive grid-based Bayesian lens-modelling code by Vegetti & Koopmans 2009a, used in this work) allowing for a simultaneous reconstruction of both the smooth lensing potential $\psi_0(\mathbf{x})$ and the original surface-brightness distribution of the background source $S(\mathbf{y})$, based on the observed surface brightness of the lensed source emission $I(\mathbf{x})$.

Compared to the observed background-source emission $I(\mathbf{x}) = S(\mathbf{x} - \nabla \psi(\mathbf{x}))$ lensed by the true lensing potential $\psi(\mathbf{x})$, the smooth-lens model of the lensed images $I_0(\mathbf{x}) = S(\mathbf{x} - \nabla \psi_0(\mathbf{x}))$ leads to a modification in the mapping between the lens- and the source plane (described by equation 6) and, thus, results in a surface-brightness change $\delta I(\mathbf{x})$ between the observed and the modelled surface brightness of the lensed source emission:

$$\delta I(\mathbf{x}) = I(\mathbf{x}) - I_0(\mathbf{x}) = S(\mathbf{x} - \nabla \psi(\mathbf{x})) - S(\mathbf{x} - \nabla \psi_0(\mathbf{x})). \quad (8)$$

In what follows, we refer to such surface-brightness discrepancies $\delta I(\mathbf{x})$, caused by a deviation of the true lensing potential $\psi(\mathbf{x})$ from the best-fitting smooth lensing potential $\psi_0(\mathbf{x})$, as *surface-brightness anomalies*. The aim of this study is to relate these observable surface-brightness anomalies, quantified in terms of their power spectrum $P_{\delta I}(k)$, to statistical properties of the underlying density perturbations in the lensing mass and, finally, infer the resulting constraints on the power spectrum of these projected density fluctuations $P_{\delta \kappa}(k)$ in the mass distribution of the studied lens galaxy.

However, in reality, the extraction of such surface-brightness anomalies arising from density fluctuations in the lens galaxy is complicated by three independent phenomena. First, observational effects make it impossible to measure the true surface-brightness distribution of the lensed images $I(\mathbf{x})$. Instead, solely the entangled effect of lensing blurred by the convolution with the point-spread function (PSF) can be observed, in the presence of the observational noise: $I(\mathbf{x}) * \text{PSF} + n(\mathbf{x})$. Second, the reconstructed best-fitting unlensed surface-brightness distribution of the background source $S_R(\mathbf{y})$ cannot be assumed to perfectly represent the true surface-brightness distribution of the source galaxy $S_T(\mathbf{y})$, owing to a degeneracy between the intrinsic surface-brightness inhomogeneities in the source galaxy itself and the gravitational imprints of possible small-scale density fluctuations in the lensing mass. Consequently, the true source structure might be suppressed or enhanced as a result

of an over- or underregularised source reconstruction in the lens-modelling procedure. In other words, the reconstructed smooth-lens model might potentially "absorb" density fluctuations present in the lensing mass into spurious source structure or, vice versa, result in artificially enhanced surface-brightness anomalies if the source reconstruction is overregularised (i.e. too smooth). Third, the effect of strong gravitational lensing is sensitive to the total mass present in the line-of-sight along which the gravitational lens is observed. Thus, the measured surface-brightness anomalies might arise not only from the investigated density fluctuations in the lens galaxy, but also from mass structure along the line-of-sight. To conclude, one of the main challenges in our approach is to extract the true surface-brightness anomalies $\delta I(\mathbf{x})$ (as defined in equation 8) from the measured total residual surface-brightness fluctuations in the lensed images: $S_T(\mathbf{x} - \nabla\psi(\mathbf{x})) * \text{PSF} - S_R(\mathbf{x} - \nabla\psi_0(\mathbf{x})) * \text{PSF} + n(\mathbf{x})$, taking into consideration all the discussed effects.

To be conservative in coping with these degeneracies, in this paper we only separate the effect of noise (Section 3.6) and treat any residual surface-brightness fluctuations deviating from noise as an upper limit to the effect caused solely by the deviation of the true lensing-mass distribution from the smooth-lens model (defined as surface-brightness anomalies) and, thus, aim at placing only an upper limit on the level of clumpiness in the total projected mass distribution of the lens galaxy. In a follow-up paper, we plan to investigate in more detail both the line-of-sight effects and the discussed degeneracy between the density fluctuations in the lensing mass and the intrinsic surface-brightness inhomogeneities in the background-source galaxy itself. Once these degeneracies are quantified, our technique will allow for a statistical detection of the entire population of low-mass density fluctuations and, thus, provide more stringent constraints on the dark-matter and galaxy-formation models, based on a comparison between the inferred properties of mass structure in the studied observed lens systems and the predictions from hydrodynamical simulations.

2.2 GRF-potential perturbations in the lens galaxy

When modelling density inhomogeneities in lens galaxies, the standard approach is to approximate the true lensing potential $\psi(\mathbf{x})$ by the best-fitting smoothly-varying parametric potential model $\psi_0(\mathbf{x})$ and treat any deviation as a potential correction $\delta\psi$ (e.g. Koopmans 2005; Vegetti & Koopmans 2009a). While previous work in this area aimed mainly at the detection of individual dark matter sub-haloes (e.g. Vegetti et al. 2012, 2014) and line-of-sight haloes (Despali et al. 2017), in this paper we investigate the departures from a smooth-lens model in general i.e. density fluctuations in the total lensing mass arising not only from CDM sub-haloes in the host halo or haloes in the line-of-sight, but also from the complex and realistic distribution of both dark and baryonic matter in the lens galaxy.

Following the statistical approach of Chatterjee & Koopmans (2018), we treat such inhomogeneities in the total lensing-mass distribution as a statistical ensemble and model the associated potential corrections in terms of a homogeneous and isotropic Gaussian potential-perturbation field $\delta\psi_{\text{GRF}}(\mathbf{x})$ (with $\langle\delta\psi_{\text{GRF}}(\mathbf{x})\rangle = 0$) superposed on a smoothly-varying lensing potential $\psi_0(\mathbf{x})$. Consequently, in what follows, we assume that the true lensing potential $\psi(\mathbf{x})$ of the considered lens galaxy can to the first order be well approximated by the sum of the best-fitting smoothly-varying parametric component $\psi_0(\mathbf{x})$ and a Gaussian potential-perturbation field $\delta\psi_{\text{GRF}}(\mathbf{x})$:

$$\psi(\mathbf{x}) \approx \psi_0(\mathbf{x}) + \delta\psi_{\text{GRF}}(\mathbf{x}), \quad (9)$$

with no covariance between $\delta\psi_{\text{GRF}}(\mathbf{x})$ and $\psi_0(\mathbf{x})$. Under this assumption, equations (3-6), relating the potential-, convergence- and the deflection-angle fields, hold for both the smooth and the perturbative mass components separately.

In particular, the deflection angle $\alpha(\mathbf{x})$ caused by such a linearly approximated lensing potential can be separated into the deflection due to the smooth lensing potential $\alpha_0(\mathbf{x})$ and the differential deflection-angle field $\delta\alpha_{\text{GRF}}(\mathbf{x})$ due to the additional lensing effect of the Gaussian potential perturbations $\delta\psi_{\text{GRF}}(\mathbf{x})$:

$$\alpha(\mathbf{x}) = \nabla\psi(\mathbf{x}) \approx \nabla\psi_0(\mathbf{x}) + \nabla\delta\psi_{\text{GRF}}(\mathbf{x}) = \alpha_0(\mathbf{x}) + \delta\alpha_{\text{GRF}}(\mathbf{x}). \quad (10)$$

The resulting differential deflection-angle field $\delta\alpha_{\text{GRF}}(\mathbf{x})$ can be in this case directly linked to the underlying potential perturbations $\delta\psi_{\text{GRF}}(\mathbf{x})$ via:

$$\delta\alpha_{\text{GRF}}(\mathbf{x}) = \nabla\delta\psi_{\text{GRF}}(\mathbf{x}), \quad (11)$$

independently of the smooth lensing component $\psi_0(\mathbf{x})$. Similarly, the convergence-perturbation field $\delta\kappa_{\text{GRF}}(\mathbf{x})$ is directly related to the corresponding potential-perturbation field $\delta\psi_{\text{GRF}}(\mathbf{x})$ via the Poisson equation:

$$\nabla^2\delta\psi_{\text{GRF}}(\mathbf{x}) = 2 \times \delta\kappa_{\text{GRF}}(\mathbf{x}). \quad (12)$$

A crucial feature of a Gaussian Random Field (GRF) is that its properties are entirely characterised by the second-order statistics. Since $\langle\delta\psi(\mathbf{x})\rangle = 0$, the statistical behaviour of the hypothetical GRF-potential perturbations $\delta\psi(\mathbf{x})$ is fully described by the 2-point correlation function or, alternatively, its Fourier transform - the power spectrum. We assume the power spectrum of the GRF potential perturbations $P_{\delta\psi}(k)$ to follow a (piecewise) featureless isotropic power law:

$$P_{\delta\psi}(k) = A \times k^{-\beta} \quad (13)$$

with two free parameters - the amplitude A , related to the total variance of the GRF-potential perturbations, and the power-law slope β , determining the distribution of this variance over the different length scales (i.e. k -modes) and, thus, describing the scale dependence of the investigated inhomogeneity pattern in the lensing-mass distribution. For further analysis, we choose the convention in which the wavenumber k , measured in arcsec^{-1} , corresponds to the reciprocal wavelength λ :

$$k \equiv \lambda^{-1} \quad (14)$$

of the associated harmonic wave $e^{-2\pi ik \cdot x}$ in the Fourier representation of the GRF field.

Our method is based on the analysis of a two-dimensional science image with a finite size L (length on a side, measured in arcsec) and its Fourier transform in the two-dimensional k -space. We assume the amplitude A and slope β to be constant over the entire investigated k -range and choose to set A by specifying the overall variance $\sigma_{\delta\psi}^2$ of the GRF fluctuations in the considered field-of-view as follows:

$$\int_{k_x} \int_{k_y} P_{\delta\psi}(A, \beta, \sqrt{k_x^2 + k_y^2}) dk_x dk_y = \sigma_{\delta\psi}^2, \quad (15)$$

where

$$\sigma_{\delta\psi}^2 \equiv \langle(\delta\psi - \langle\delta\psi\rangle)^2\rangle = \langle\delta\psi^2\rangle, \quad (16)$$

wavenumbers k_x and k_y are calculated according to equation (14) and the integration is performed over the corresponding Fourier grid. Substituting $P_{\delta\psi}(k)$ in equation (15) with equation (13) and replacing the integrals by a summation over discrete pixels with the size $dk_x = dk_y = L^{-1}$ in k -space leads to the final normalisation

condition for the amplitude of the power-law power spectrum (equation 13) with given values for the slope β and the variance $\sigma_{\delta\psi}^2$:

$$A(\sigma_{\delta\psi}^2, \beta, L) = \frac{L^2 \sigma_{\delta\psi}^2}{\sum_{k_x} \sum_{k_y} (\sqrt{k_x^2 + k_y^2})^{-\beta}}. \quad (17)$$

As can be seen from equation (17), this normalisation depends on the chosen field-of-view and the pixel grid of the analysed image.

The methodology presented in this work aims at deriving observational upper-limit constraints on the two free parameters uniquely characterising the statistical nature of the investigated hypothetical GRF-potential perturbations $\delta\psi_{\text{GRF}}(\mathbf{x})$: the variance $\sigma_{\delta\psi}^2$ and the slope β of the assumed underlying power-law power spectrum $P_{\delta\psi}(k)$, as defined in equations (13-17). To accomplish this goal, we use the fact that perturbing the best-fitting smoothly-varying lensing potential $\psi_0(\mathbf{x})$ with GRF-potential fluctuations $\delta\psi_{\text{GRF}}(\mathbf{x})$ results in a differential deflection $\delta\alpha_{\text{GRF}}(\mathbf{x})$ of the light rays from the background source, see equation (11). Due to the associated modification in the mapping between the lens- and the source plane (described by equation 6), this additional lensing effect leads to perturbations $\delta I_{\text{GRF}}(\mathbf{x})$ in the surface-brightness distribution of the lensed images with respect to the smooth-lens model $I_0(\mathbf{x})$:

$$\begin{aligned} \delta I_{\text{GRF}}(\mathbf{x}) &= I_{\text{GRF}}(\mathbf{x}) - I_0(\mathbf{x}) = \\ &= S(\mathbf{x} - \nabla\psi_0(\mathbf{x}) - \nabla\delta\psi_{\text{GRF}}(\mathbf{x})) - S(\mathbf{x} - \nabla\psi_0(\mathbf{x})) = \\ &= S(\mathbf{x} - \alpha_0(\mathbf{x}) - \delta\alpha_{\text{GRF}}(\mathbf{x})) - S(\mathbf{x} - \alpha_0(\mathbf{x})), \end{aligned} \quad (18)$$

as explained in Section 2.1.

In order to test whether the surface-brightness anomalies observed in real lens systems can be explained by such a differential deflection due to GRF-potential perturbations in the lens galaxy, we perturb the best-fitting smoothly-varying lensing potential $\psi_0(\mathbf{x})$ with GRF-potential fluctuations $\delta\psi_{\text{GRF}}(\mathbf{x})$ generated from the assumed power-law power spectrum with specific values for the variance $\sigma_{\delta\psi}^2$ and the slope β , and subsequently compare the resulting surface-brightness change $\delta I_{\text{GRF}}(\mathbf{x})$ in the simulated perturbed lensed images with the observed surface-brightness anomalies. We perform such simulations for an entire set of different combinations of $\sigma_{\delta\psi}^2$ and β , in what follows referred to as *matter power-spectrum models*, and quantify the results of this comparison in terms of the exclusion probability for each of the considered matter power-spectrum models (see Section 3.9).

For a comparison with theoretical predictions, these results can be translated into constraints on the corresponding power spectrum of the convergence perturbations $P_{\delta\kappa}(k)$ or, alternatively, the power spectrum of perturbations in the deflection angle $P_{\delta\alpha}(k)$. To perform this conversion, we express equations (10) and (12) in the Fourier space, following the chosen Fourier convention defined in equation (14). As a result, the deflection power spectrum $P_{\delta\alpha}(k)$ can be related to the underlying power spectrum of the potential perturbations $P_{\delta\psi}(k)$ as follows:

$$P_{\delta\alpha}(k) = 4\pi^2 k^2 P_{\delta\psi}(k). \quad (19)$$

The convergence-power spectrum $P_{\delta\kappa}(k)$ and the power spectrum of the corresponding potential perturbations $P_{\delta\psi}(k)$ are linked via the following relation:

$$P_{\delta\kappa}(k) = 4\pi^4 k^4 P_{\delta\psi}(k). \quad (20)$$

In the final interpretation, we express the inferred constraints in terms of the more commonly used dimensionless convergence-power spectrum:

$$\Delta_{\delta\kappa}^2(k) \equiv 2\pi k^2 P_{\delta\kappa}(k) \quad (21)$$

which measures the contribution of a particular length scale $\lambda = k^{-1}$ to the total variance of the convergence perturbations (surface-mass density perturbations in units of the critical surface-mass density Σ_{cr} for the considered lens system). For completeness, we additionally present the corresponding constraints on the dimensionless deflection power spectrum $\Delta_{\delta\alpha}^2(k)$ defined as:

$$\Delta_{\delta\alpha}^2(k) \equiv 2\pi k^2 P_{\delta\alpha}(k). \quad (22)$$

We emphasize that we intend to apply our method solely to lens systems for which single localised sub-haloes and satellite galaxies were either already detected and modelled separately, or excluded by previous research. Moreover, in the future, we plan to additionally use hydrodynamical simulations to thoroughly test the validity of the Gaussianity assumption in our description of the hypothetical departures from the best-fitting smooth model in the investigated total mass distribution of massive elliptical (lens) galaxies.

2.3 Analysis overview

Our approach to constrain the level of mass clumpiness on sub-galactic scales consists of the following three crucial components, briefly discussed below.

- First, we extract and quantify the statistical properties of surface-brightness anomalies in the lensed images of the observed galaxy-galaxy strong gravitational lens system. For this, we measure the one-dimensional azimuthally-averaged power spectrum $P_{\delta I}(k)$ of residual surface-brightness fluctuations remaining in the lensed images after the lens-galaxy subtraction, the smooth-lens modelling and the noise correction. This observational measurement includes the following steps:

- (i) HST observations and data reduction by means of the DRIZ-ZLEPAC package (Gonzaga et al. 2012), see Sections 3.1 and 3.2;
- (ii) modelling and subtraction of the smooth surface-brightness contribution from the foreground lens galaxy using GALFIT (Peng et al. 2002), see Section 3.3;
- (iii) simultaneous reconstruction of the smooth lensing potential $\psi_0(\mathbf{x})$, the unlensed surface-brightness distribution of the background source galaxy $S(\mathbf{y})$ and the smooth-lens model of the lensed images $I_0(\mathbf{x})$ by means of the adaptive and grid-based Bayesian lens-modelling technique by Vegetti & Koopmans (2009a), see Section 3.4;
- (iv) statistical quantification of the residual surface-brightness fluctuations in the lensed images in terms of the one-dimensional azimuthally-averaged power spectrum $P_{\delta I}(k)$, see Section 3.5;
- (v) estimation of the noise-power spectrum and correction for the noise contribution (both sky background and the flux-dependent photon shot noise) to the power spectrum of the revealed total residual surface-brightness fluctuations, see Section 3.6.

A performance test of this procedure on mock lensed images mimicking the studied lens system, described in Section 3.7, allows us to optimise the choice of different options in the smooth-lens modelling procedure and the most suitable wavenumber range for the analysed power spectra.

- Second, we generate comparable mock realisations of surface-brightness anomalies caused by GRF-potential perturbations $\delta\psi_{\text{GRF}}(\mathbf{x})$ with known statistical properties. To achieve this goal, we apply the GRF formalism introduced in Section 2.2 and simulate realisations of GRF-potential perturbations with the desired

variance $\sigma_{\delta\psi}^2$ and the power-law slope β from the underlying GRF power spectrum $P_{\delta\psi}(k)$, as defined in equations (13-17). Superposing these realisations on the best-fitting smooth lensing potential $\psi_0(\mathbf{x})$ and repeating the lensing operation of the background-source light $S(\mathbf{y})$ with the perturbed lensing potential $\psi_0(\mathbf{x}) + \delta\psi_{\text{GRF}}(\mathbf{x})$ enables us to create realistic mock perturbed lensed images, mimicking the analysed real system, which can be subsequently compared with the observed data. For this comparison, we create a grid in the parameter space $\sigma_{\delta\psi}^2 - \beta$, containing different combinations of values for the variance and the power-law slope, and simulate mock perturbed lensed images for each point of this grid. This procedure allows us to map the statistical properties of the superposed perturbing GRF-potential fluctuations, uniquely characterised by $\sigma_{\delta\psi}^2$ and β , on the corresponding power spectra of the resulting surface-brightness anomalies in the perturbed lensed images $P_{\delta I}(k)$; see Section 3.8.

- Third, we infer upper-limit constraints on the sub-galactic convergence-power spectrum based on a statistical comparison of the measured with the mock surface-brightness anomalies. For this, we compare the power spectrum of the mock surface-brightness anomalies $P_{\delta I}(k)$ assigned to each point of the $\sigma_{\delta\psi}^2 - \beta$ grid (matter-power spectrum model) to the power spectrum of the surface-brightness anomalies measured in our observations and calculate the resulting probability of model exclusion given the measured data, see Section 3.9. The inferred constraints on the power spectrum of the studied GRF-potential perturbations $P_{\delta\psi}(k)$ are finally expressed in terms of the power spectra for the corresponding perturbations in the convergence $P_{\delta\kappa}(k)$ and the differential deflection angle $P_{\delta\alpha}(k)$; see Section 4.

In the following Section 3, our methodology is explained in more detail and illustrated by applying it, as a pilot project, to the galaxy-galaxy strong gravitational lens system SDSS J0252+0039 from the SLACS Survey.

3 APPLICATION TO HST-IMAGING OF SDSS J0252+0039

With the aim of testing and illustrating our methodology, in this section we apply it to HST-imaging of SDSS J0252+0039, one of only ten galaxy-galaxy strong gravitational lens systems from the SLACS Survey with deep UV HST/WFC3/F390W-imaging data (referred to as *U-band* in the remainder of the paper). The chosen system consists of a massive elliptical galaxy at redshift $z_l = 0.280$ acting as a gravitational lens on a blue star-forming source galaxy at redshift $z_s = 0.982$ (Bolton et al. 2008). Besides the high mass of the lens galaxy and the clumpiness of the star-forming background source, allowing us to increase the sensitivity of our method, the relatively simple lens geometry of SDSS J0252+0039 makes it a good choice for illustrating and testing our new approach.

As one of the SLACS gravitational lens systems, SDSS J0252+0039 has already been studied based on HST observations at near-infrared (in F160W: Program 11202, PI Koopmans) and optical wavelengths (in F814W: Program 10866, PI Bolton and in F606W: Program 11202, PI Koopmans), see Bolton et al. (2008); Auger et al. (2009, 2010). In particular, Vegetti et al. (2014) applied the technique of direct gravitational imaging (Koopmans 2005; Vegetti & Koopmans 2009a) to HST/ACS data of SDSS J0252+0039 in the V- and I-bands in search of the possible single halo structure in its lens galaxy. However, no gravitational signatures of localised substructure were identified above the mass-detection threshold. Here we make use of deep U-band HST/WFC3/F390W-observations with

a higher resolution and sensitivity to surface-brightness anomalies in the lensed images, which allows us to search for collectively-induced gravitational imprints of much smaller fluctuations in the total mass distribution of the lens galaxy.

3.1 Observational strategy

The mass of the smallest density fluctuations that can be (indirectly) detected in a galaxy-scale halo using the method of gravitational imaging (Koopmans 2005; Vegetti & Koopmans 2009a) is limited by the sensitivity of the observational setup to tiny surface-brightness fluctuations in the lensed images. However, as argued by Blandford et al. (2001) and Koopmans (2005), and explicitly demonstrated by Rau et al. (2013), the surface-brightness perturbations arising in the lensed images due to a given density fluctuation in the lens galaxy are enhanced when observed in a lens system with a bright compact or highly structured background source. Thus, due to the fact that, compared to the smooth old stellar populations seen in the optical and infrared bands, the source surface brightness is considerably more structured in the UV owing to the clumpy star-forming regions observable in this band, performing the analysis in the U-band can substantially improve the overall sensitivity of our approach to small density fluctuations in the lensing mass.

The idea of studying blue source galaxies with a high star-formation rate lensed by massive early-type galaxies was observationally followed up in the *Discovering the Dark Side of CDM Substructure* program (Program 12898, PI Koopmans). Aiming at detecting and quantifying possible surface-brightness anomalies in the lensed clumpy star-forming regions of the source galaxies, a sub-sample of ten SLACS galaxy-scale gravitational lens systems with the brightest and most extended high-S/N lensed images, including SDSS J0252+0039 investigated in this work, was selected for deep HST/WFC3/F390W follow-up observations. While the choice of the U-band increases the sensitivity of our method to low-mass density fluctuations, at the same time it potentially complicates the reconstruction of the background-source surface-brightness distribution, by introducing a stronger degeneracy between the complex surface-brightness structure of the source and the investigated deviation of the true lensing potential from the best-fitting smooth model. We plan to investigate this issue in more detail in a follow-up paper.

3.2 Observations and data reduction

The deep HST/WFC3/F390W observations of SDSS J0252+0039 were taken on August 25, 2013. For our study, we retrieve the observed eight dithered flat-field calibrated images from the MAST archive¹ and use the drizzle method to combine them into the final science image. We perform the drizzling by means of the `ASTRODRIZZLE` task from the `DRIZZLEPAC` package (Gonzaga et al. 2012) in its default configuration, with the original HST/WFC3 rotation, the output-pixel size of 0.0396 arcsec and the drop size equal to the original pixel size (*final pixfrac* = 1). The following analysis is carried out based on a cutout from this image with the size of 121 by 121 pixels (corresponding to an area of 4.48 arcsec on a side), centered on the brightest pixel of the lensing galaxy; see Fig. 1.

As discussed in more detail in Appendix A, the drizzling procedure is known to lead to correlations of adjacent pixels in the final drizzled science image (for a more detailed explanation see Casertano et al. 2000). This correlation is additionally enhanced by the

¹ <http://archive.stsci.edu/hst/search.php>

charge-transfer inefficiency (CTI) of the HST/WFC3/UVIS-CCDs (see e.g. Baggett et al. 2015). In order to investigate and possibly suppress these instrumental effects, in Appendix A we carry out the drizzling procedure with different settings and compare the results to those obtained with the default parameter values. Moreover, we investigate the effect of the charge-transfer inefficiency in the HST/WFC3/UVIS CCDs by comparing the power spectra of empty-sky cutouts (located in vicinity to the studied lens system) obtained by drizzling either the original or the CTI-corrected flat-field calibrated exposures, retrieved from the MAST archive. Based on this analysis, we finally decide to proceed our study in the default configuration of the drizzling procedure and without correcting for the CTI.

To account for further observational effects present in the science image, we obtain the Point-Spread-Function (PSF) of the HST/WFC3/UVIS optics using the PSF-modelling software TINYTIM² (Krist et al. 2010), with the approximation of the G8V spectral type for the lensing galaxy (based on its known magnitudes in the V-, I- and H-bands from Auger et al. 2009). Even though the TinyTim-PSF might not be a perfect representation of the real telescope optics, which is a potential source of bias in our analysis, the possible minor deviations from the true PSF would affect the measured power spectra of the residual surface-brightness fluctuations only on scales below the full width at half maximum (FWHM) of the PSF, corresponding to wavenumbers $k \gtrsim \text{FWHM}^{-1} = (0.07 \text{ arcsec})^{-1} \approx 14 \text{ arcsec}^{-1}$, well beyond the regime considered in this work (see Section 3.6).

Additionally, for visual purposes and in order to assess the possible presence of dust in the studied lens system, we apply the STIFF³ software to create a false-colour image of SDSS J0252+0039, see Fig. 2, showing a smooth early-type lens galaxy and uniformly blue lensed images of a background-source galaxy. A visual inspection shows no indication for dust extinction either in the lens or the source galaxy. A more quantitative dust analysis, based on the created U-I image, is presented in Appendix B and finds no evidence for dust extinction in the lens galaxy.

3.3 Lens-galaxy subtraction

The observed image of the galaxy-galaxy strong gravitational lens system SDSS J0252+0039 (Fig. 1) contains contributions from both the foreground lens- and the background lensed source galaxy, which leads to an overlap between the lensed emission of the background galaxy and the inner region of the foreground massive elliptical lens galaxy – the angular distance of nearly 1 arcsec between the gravitational arcs and the lens-galaxy centre is slightly lower than the effective radius of the lens galaxy. However, at the positions of the lensed images, we expect the total measured surface-brightness to be dominated by the contribution of the lensed images (see Fig. 3). Assuming that the surface brightness of the lens galaxy is smoothly distributed, these two contributions can be disentangled by modelling and subtracting the best-fitting smooth surface-brightness distribution of the lens galaxy from the original science image (see e.g. Bolton et al. 2006). For early-type galaxies, the most widely used parameterised class of smooth light profiles is the Sérsic profile (Sérsic 1963).

We follow this approach and model the surface-brightness distribution of the massive elliptical lens galaxy in SDSS J0252+0039

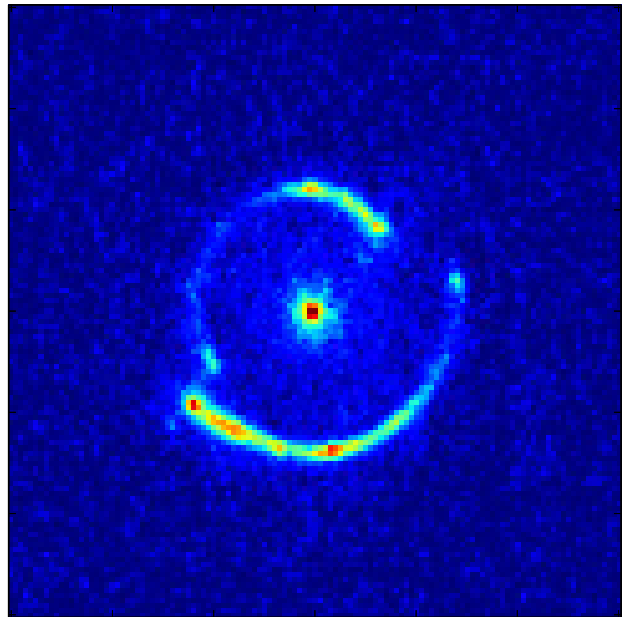


Figure 1. HST imaging of the galaxy-galaxy strong gravitational lens system SDSS J0252+0039: the analysed HST/WFC3/F390W drizzled science image, corresponding to an area of 4.48 arcsec on a side.

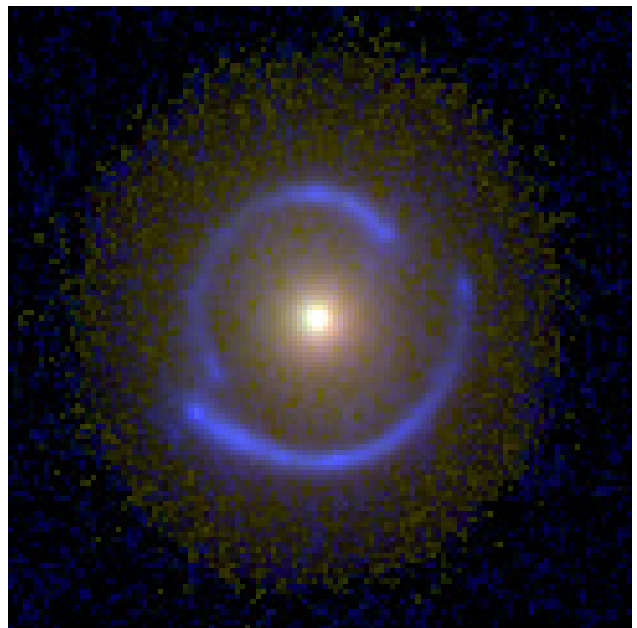


Figure 2. Colour-composite image of the galaxy-galaxy strong gravitational lens system SDSS J0252+0039 based on the HST/WFC3/F390W U-band photometry (blue) combined with HST-observations in the visual (F814W; green) and infrared bands (F160W; red) using the STIFF software.

using the two-dimensional fitting algorithm GALFIT (Peng et al. 2002) after masking out all pixels covering the lensed images, see Fig. 3. The obtained best-fitting GALFIT model consists of two Sérsic components with Sérsic indices $n = 4.44$ and $n = 0.09$ and effective radii 1.2 and 0.96 arcsec (corresponding to ~ 4.8 and ~ 3.8 kpc at the redshift of the lens), respectively. The small value of the second Sérsic index suggests that the light distribution of the lensing galaxy

² <http://www.stsci.edu/hst/observatory/focus/TinyTim>

³ <https://www.astromatic.net/software/stiff>

can be well described by a diffuse stellar halo around a standard de-Vaucouleurs profile. As an alternative, we additionally carry out the lens-galaxy subtraction using the B-SPLINE algorithm, developed by Bolton et al. (2006), but decide to continue our analysis based on the GALFIT model due to a slightly higher Bayesian evidence of the resulting best-fitting smooth-lens model, see Section 3.4.

The final lens-galaxy subtracted image (see Fig. 3), created by subtracting the GALFIT model of the lens galaxy from the original science image, contains only the lensed emission of the background-source galaxy and as such can be used for the smooth-lens modelling of the studied lens system, discussed in the following section.

3.4 Smooth-lens modelling

In search of the surface-brightness anomalies arising in the lensed images due to the presence of the investigated hypothetical density inhomogeneities in the total mass distribution of the foreground lens galaxy, we initially model the studied lens system assuming that the lensing-mass distribution is smooth and well described by the power-law elliptical mass-distribution model (PEMD, Barkana 1998) in an external shear field.

3.4.1 Lens-modelling technique

The smooth-lens modelling is performed using the adaptive and grid-based Bayesian lens-modelling technique of Vegetti & Koopmans (2009a). This method allows us to simultaneously reconstruct both the unlensed background-source surface-brightness distribution $S(y)$ on an adaptive grid in the source plane and the best-fitting smoothly-varying mass-density distribution of the foreground galaxy projected onto the lens plane. The modelled smooth surface-mass density of the lens galaxy as a function of the position in the lens plane is parametrised in terms of the convergence κ (defined in equation 2) in the following way:

$$\kappa(x, y) = \frac{b(2 - \frac{\gamma}{2})q^{\gamma-3/2}}{2(x^2q^2 + y^2)^{(\gamma-1)/2}} \quad (23)$$

with the following free parameters – the lens strength b , the position angle θ , the axis ratio q , the (three-dimensional) mass-density slope γ ($\gamma = 2$ in the isothermal case), the centre coordinates of the lensing-mass distribution in the lens plane x_0 and y_0 , the external shear strength Γ and its position angle Γ_θ , as introduced by Vegetti & Koopmans (2009a).

The applied smooth-lens modelling algorithm by Vegetti & Koopmans (2009a) includes several options for the inversion of the lensing operation and the resulting reconstruction of the original source surface-brightness distribution: adaptive or non-adaptive, variance, gradient or curvature source-plane regularization as well as a variable source-grid resolution (characterised by the number n and spacing of the pixels cast back from the lens plane to the source plane). As pointed out by Vegetti et al. (2014) and Suyu et al. (2006), the optimal choice for the number of pixels n and the form of the source regularisation used in the smooth-lens modelling depends crucially on the smoothness of the modelled lensed images and may vary from system to system. Thus, the common practice is to perform the smooth-lens modelling with different combinations of the above options and choose the optimal settings based on the highest marginalized Bayesian evidence.

Table 1. Parameter values of the best-fitting smooth lensing-mass distribution for SDSS J0252+0039 obtained in the U-band (F390W) in comparison to the values from the I-band (F814W) reconstruction by Vegetti et al. (2014). Following Vegetti & Koopmans (2009a), the gravitational potential of the lensing galaxy was modelled as a power-law elliptical mass distribution with the following set of free parameters: the lens strength b , the position angle θ (with respect to the original telescope rotation), the axis ratio q , the slope of the projected lensing mass density γ , the external shear strength Γ and its position angle Γ_θ . In both bands, the reconstruction was carried out using the adaptive gradient source regularization and casting back each pixel ($n = 1$).

Filter	b ["]	θ [deg.]	q	γ	Γ	Γ_θ [deg.]
F390W	0.996	150.1	0.978	2.066	-0.015	81.4
F814W	1.022	26.2	0.943	2.047	0.009	101.8

3.4.2 Best-fitting smooth-lens model for SDSS J0252+0039

Based on the analysed F390W-data (U-band), the projected mass distribution of the lens galaxy in SDSS J0252+0039 is best modelled as PEMD with the parameter values listed in Table 1, in a good agreement with the corresponding best-fitting smooth model found by Vegetti et al. (2014) based on the F814W-data (I-band), except from the apparent discrepancy in the position angle θ between the presented smooth-lens models in the U- and I-band. This discrepancy can be explained by the rotational invariance owing to the nearly spherical symmetry of the modelled lensing-mass distribution (axis ratio q very close to 1) and the negligible external shear Γ , hardly altering the lensing potential. Furthermore, the best-fitting parameter values of the smooth-lens models in both bands (see Table 1) indicate a nearly isothermal mass-density profile ($\gamma \approx 2$), which together with the previous considerations leads to the conclusion that SDSS J0252+0039 is well described by a Singular Isothermal Sphere (SIS) model with the Einstein radius $\Theta_E \approx b \approx 1$ arcsec.

3.4.3 Degeneracies in the smooth-lens modelling

Whereas the particular choice for the number of pixels n cast back from the lens plane to the source plane, the form of the source regularisation and the size of the mask covering the lensed images hardly affects the best-fitting parameter values of the lensing potential, we find that it has a significant effect on the reconstructed unlensed surface-brightness distribution of the background-source galaxy and, thus, the level of the residual surface-brightness fluctuations remaining in the lensed images after the best-fitting model has been subtracted. Among all the available options combined with the chosen mask (depicted in Fig. 3), the highest value of the marginalized Bayesian evidence is achieved when modelling the F390-data of SDSS J0252+0039 with the adaptive gradient source-grid regularization and casting back each pixel from the lens plane to the source plane (referred to as $n = 1$).

However, despite a remarkably good agreement between the observed lensed images $I(x)$ and the reconstructed smooth-lens model of the lensed emission $I_0(x)$, the obtained source reconstruction turns out to be under-regularised – all surface-brightness fluctuations present in the lensed images and even part of the noise have been "absorbed" in the source structure. As can be seen in Fig. 6, the power spectrum of the residual surface-brightness fluctuations (measured and discussed in Section 3.5) remaining in the lensed images after subtraction of the best-fitting smooth-lens model with $n = 1$ lies below the noise-power spectrum (estimated and dis-

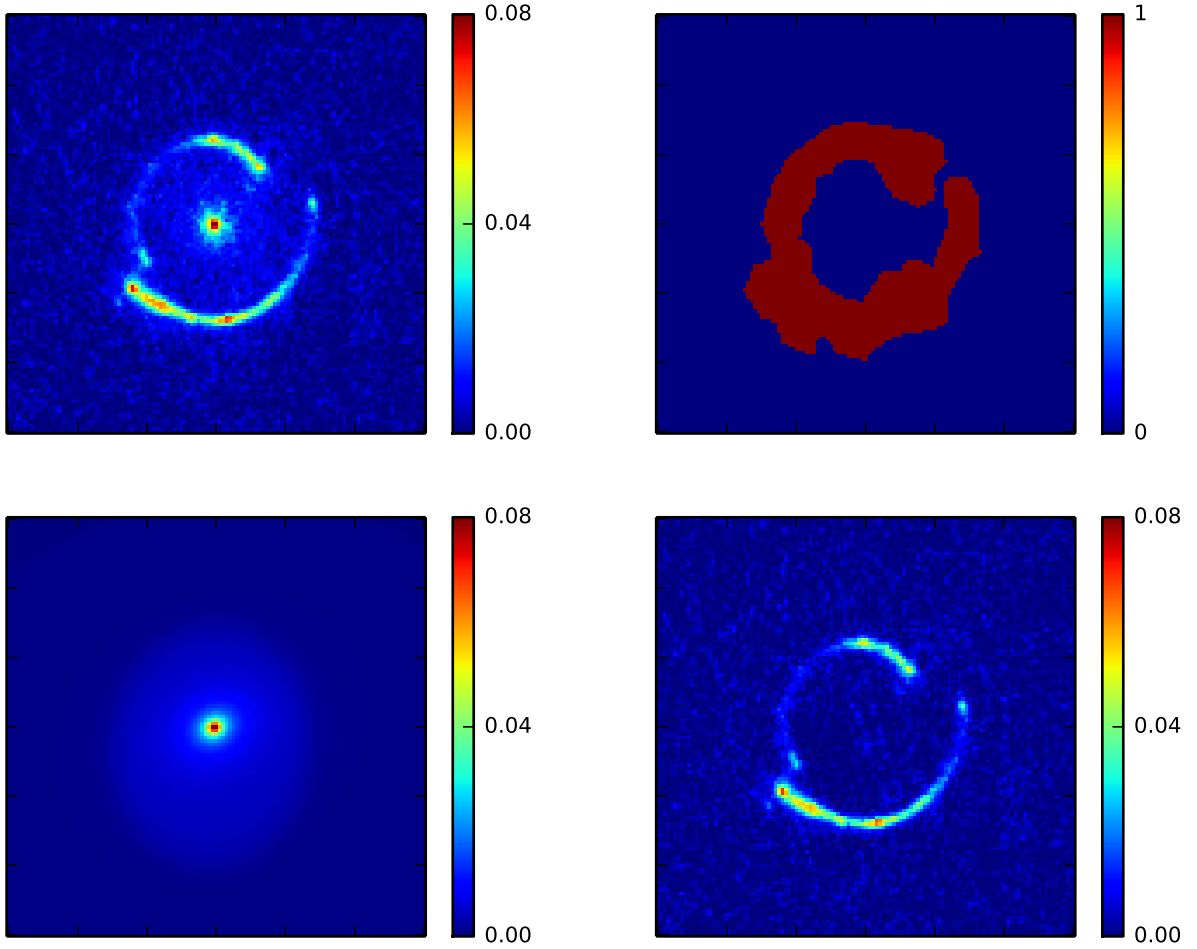


Figure 3. Lens-galaxy subtraction for SDSS J0252+0039 using *GALFIT*. *Top row:* the analysed drizzled science image in the U-band (*left panel*) and the applied mask covering the lensed source emission (*right panel*). *Bottom row:* the best-fitting *GALFIT* model of the surface-brightness distribution in the lens galaxy (*left panel*) and the lens-galaxy subtracted residual image (*right panel*).

cussed in Section 3.6) for both adaptive and non-adaptive source-grid regularisation. From this revealed overfitting we conclude that if the smooth-lens modelling of SDSS J0252+0039 in the U-band is carried out with the highest resolution (i.e. by casting back each pixel from the lens plane to the source plane; $n = 1$) and the chosen relatively tight mask, the inversion problem to be solved is under-constrained and degenerate. As discussed in Section 2.1, such a degeneracy between the surface-brightness perturbations due to density fluctuations in the lens, on the one hand, and the intrinsic structure in the source galaxy, on the other hand, bears the possibility for the smooth-lens modelling algorithm to incorrectly attribute the residual surface-brightness fluctuations caused by density inhomogeneities in the lensing mass of the foreground galaxy to spurious intrinsic structure in the surface-brightness of the background-source galaxy. Due to the enhanced intrinsic source-galaxy structure observable in the U-band, this problem is much more severe in our analysis of the F390W-data than it was the case for the I-band data previously modelled by [Vegetti et al. \(2014\)](#). Whereas the degeneracy is less problematic when trying to identify individual sub-haloes with masses above the detection limit as in [Vegetti et al. \(2014\)](#), alleviating it is a key issue in our statistical analysis of the entire population of lower-mass density fluctuations.

While a thorough analysis of the degeneracy between the

source and the potential, faced during the smooth-lens modelling, is planned to be subject of a future work, in the present paper we investigate this problem by performing additional tests for a simulated mock lens system mimicking the analysed U-band observations of SDSS J0252+0039 (see Section 3.7 and Fig. 8). Modelling a simulated lens system has the advantage that both the true unlensed surface-brightness distribution of the mock background source and the perturbing mass-density fluctuations in the mock lens galaxy are known. Our tests, discussed in Section 3.7, suggest that the degeneracy becomes less severe when the smooth lens-modelling is performed with higher values of n (lower source-grid resolution of the reconstruction). As can be seen from Fig. 8, lowering the resolution of the mock source reconstruction allows us to successfully suppress the fitting of spurious source structure and alleviate the degeneracy between the hypothetical density fluctuations in the lens and the intrinsic structure in the source galaxy.

As a further complication, the reconstructed surface-brightness distribution of the background source depends on the particular choice of the mask encompassing all the pixels taken into account in the smooth-lens modelling procedure, see Fig. 6. In this case, the outcome of the modelling cannot be compared in terms of the Bayesian evidence, since models with different masks need to be considered as based on different datasets. Our tests with different

mask sizes used for the smooth-lens modelling of the studied lens system indicate that increasing the size of the mask, in combination with a high non-adaptive source-grid regularisation, is a good alternative to lowering the source-grid resolution (increasing n) when dealing with an overfitting of the source reconstruction. From Fig. 6 it is apparent that these two options lead to very similar results for the investigated power spectrum of the residual surface-brightness fluctuations. The small difference between these power spectra in the lowest analysed k -bin does not affect our final results (exclusion probabilities for the considered matter-power spectrum models) significantly, as proved in a performed test.

Hence, taking the computational speed of our method into consideration, we continue our study based on the (more conservative) smooth-lens model with the original smaller mask and a lower source-grid resolution ($n = 3$, i.e. casting back only one pixel out of each contiguous 3×3 -pixel area), while keeping fixed the previously obtained parameter values of the best-fitting smooth lensing-mass distribution. The particular choice of $n = 3$ is motivated by the results of our simulations carried out for the mock lens system mimicking SDSS J0252+0039, discussed in Section 3.7.

3.5 Power spectrum of the residual surface-brightness fluctuations in the lensed images

After obtaining the smooth-lens model of the investigated lens system, the reconstructed unlensed surface-brightness distribution of its background galaxy $S(\mathbf{y})$ is lensed again by the best-fitting smoothly-varying lensing-mass distribution, as demonstrated in Fig. 4. The resulting smooth-lens model of the lensed emission $I_0(\mathbf{x})$, which would be observed if the lensing-mass distribution was indeed smooth, is removed from the observed data to uncover residual surface-brightness fluctuations, possibly indicating a discrepancy between the true and the assumed smooth (PEMD) lensing-mass distribution. As can be seen from Fig. 4, the residual image of SDSS J0252+0039 from the chosen lower-resolution smooth-lens modelling with $n = 3$ exhibits significant residual surface-brightness fluctuations above the noise level (see Fig. 5 for the signal-to-noise ratio image) that are now subject of a further statistical analysis.

In order to quantify these surface-brightness fluctuations, remaining in the lensed images of the analysed lens system after the lens-galaxy subtraction and the smooth-lens modelling, we determine the one-dimensional azimuthally-averaged power spectrum of the residual image within the mask covering the lensed images (initially created for the lens-galaxy subtraction in Section 3.3, as shown in Fig. 3). To achieve this, we set the flux values of the pixels located outside the mask to zero and use the Python package `NUMPY.FFT`⁴ to compute the two-dimensional discrete Fourier transform (DFT) of the masked residual image. Based on this Fourier-transformed residual image, we calculate the corresponding two-dimensional power spectrum as the squared magnitude of the (complex-valued) Fourier coefficients assigned to each pixel. Finally, assuming isotropy of the underlying potential perturbations $\delta\psi(\mathbf{x})$, we average these two-dimensional power-spectrum values along a set of ten equidistant concentric annuli covering the full Fourier-transformed image and spanning the perturbation-wavenumber range between $k_{\min} = 0.88$ and $k_{\max} = 16.79 \text{ arcsec}^{-1}$ (corresponding to the wavelength range between $\lambda_{\min} = 0.06$ and $\lambda_{\max} = 1.13 \text{ arcsec}$ or, expressed in physical units, between $\lambda_{\min} = 0.22$ and $\lambda_{\max} = 4.65 \text{ kpc}$ at

the redshift of the lens galaxy $z_l = 0.280$). The resulting one-dimensional azimuthally-averaged power spectrum of the residual surface-brightness fluctuations $P_{\delta I}(k)$ revealed in the lensed images of SDSS J0252+0039 as a function of the perturbation wavenumber k (measured in arcsec^{-1}) is presented in Fig. 6.

As discussed in Section 2.1, the residual surface-brightness fluctuations remaining in the lensed images after the smooth-lens modelling can possibly be explained by three independent phenomena. First, they could be traced back to a possible deviation of the real lensing-mass distribution from the reconstructed best-fitting PEMD model, which we intend to study and refer to as surface-brightness anomalies. Second, they might be caused by systematic model errors, such as uncertainties in the PSF model of the telescope optics or possible intrinsic structure in the lensed source, not recovered in the lens-modelling procedure due to the over-regularisation of the source reconstruction when casting back only one pixel out of each contiguous 3×3 -pixel area ($n = 3$). Third, the residual surface-brightness fluctuations can be partially attributed to the observational noise present in the analysed image. Thus, in order to constrain the surface-brightness anomalies resulting solely from the density fluctuations in the lensing mass distribution, it is crucial to investigate the possible systematic model errors (see Sections 2.1, 3.4.3 and 3.7) and separate the effect of observational noise (see Section 3.6). In the next section, we discuss how the noise contribution is estimated and corrected for based on power spectra of selected (modified) empty-sky cutouts from the original full-sky image, located in proximity to the studied lens system.

3.6 Noise-power spectrum

With the aim to characterise the noise properties in the observed HST/WFC3/F390W image of SDSS J0252+0039, we create a sample of 20 selected empty-sky regions located in proximity to the studied lens system, with the same size as the science image analysed in this paper (121 by 121 pixels). The first rough estimate of the noise level is given by the standard deviation of the flux values in this empty-sky sample: $\sigma_{sky} = 0.002 \text{ e}^- \text{ sec}^{-1}$. However, this estimate does not take into account the photon-shot (Poisson-distributed) noise, which depends on the number of detected photons and consequently varies from pixel to pixel in our observed image.

A more precise description of noise properties, including both the sky-background and the photon-shot noise, is provided by the noise-sigma map, which quantifies the standard deviation of noise for each pixel separately. Considering that the Poisson variance of the photon counts is to a good approximation equal to the measured number of photons and the raw HST images of the lens are drizzle-combined using an inverse-variance map weighting, we construct the noise-sigma map for our drizzled HST science image according to the following formula:

$$\sigma_n = \sqrt{N/W + \sigma_{sky}^2}, \quad (24)$$

where N is the number of photo-electrons per second detected in a particular pixel (after the sky-background subtraction) and W is the weight of this pixel taken from the weight map of our image provided by the drizzling pipeline. This noise-sigma map is also used in the smooth-lens modelling procedure, presented in Section 3.4, to account for noise fluctuations in the modelled lensed images. Since the Poisson noise approaches Gaussian noise for large number counts, as is the case for the studied image, in the remaining part of our analysis we approximate the photon-shot noise by an additive

⁴ <https://docs.scipy.org/doc/numpy/reference/routines.fft.html>

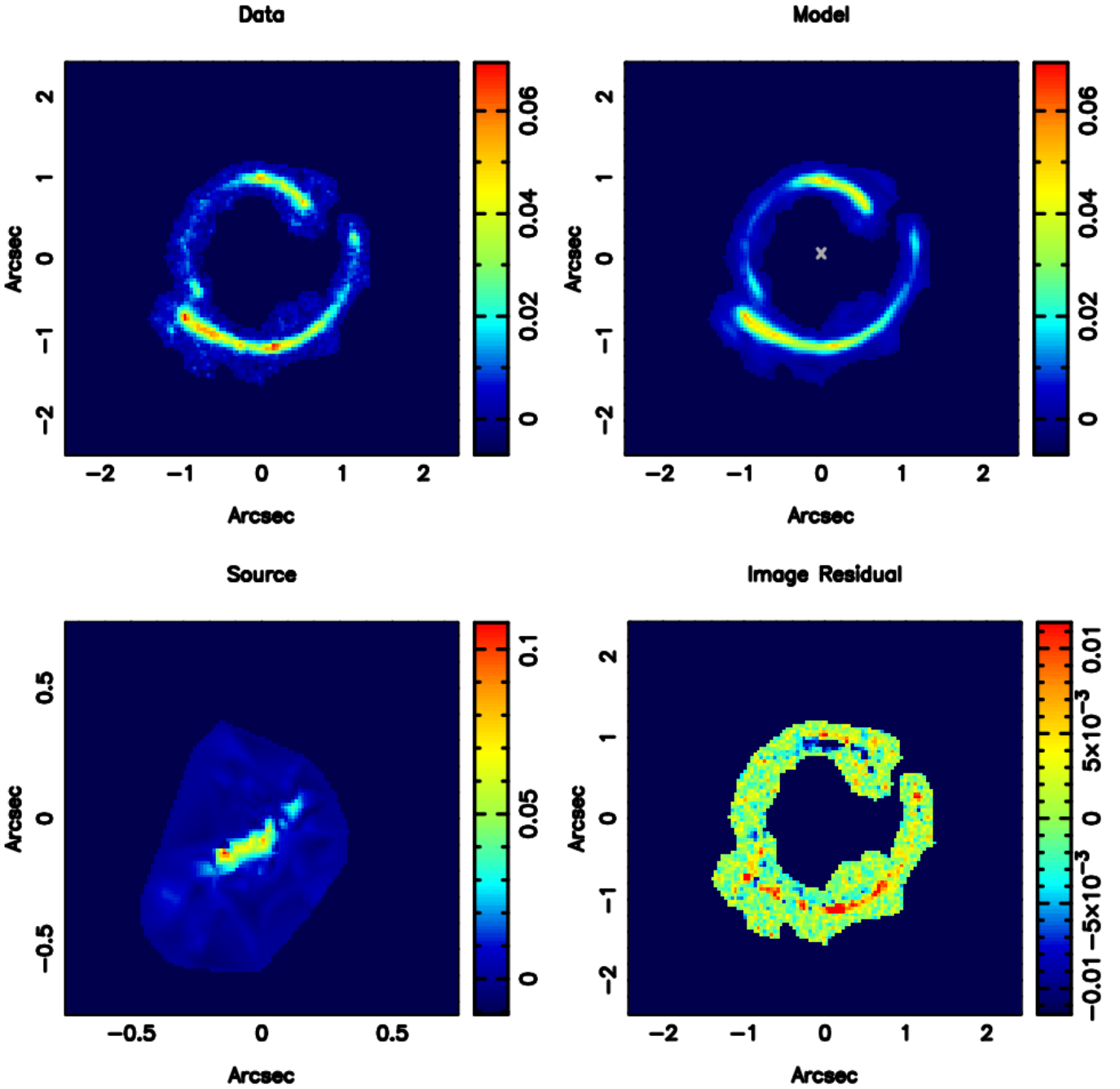


Figure 4. Smooth-lens modelling of SDSS J0252+0039 in the U-band (HST/WFC3/F390W) by means of the adaptive and grid-based Bayesian lens-modelling technique of [Vegetti & Koopmans \(2009a\)](#). To suppress the possible degeneracy between the surface-brightness anomalies due to mass structure in the lens and the intrinsic surface-brightness fluctuations in the background-source galaxy, only one pixel out of each contiguous 3×3 -pixel area is cast back from the lens to the source plane ($n = 3$). *Top row:* the lens-galaxy subtracted image overlaid with a mask, used as input for the smooth-lens modelling (*left panel*), and the final reconstructed smooth-lens model of the lensed source emission (*right panel*). *Bottom row:* the reconstructed unlensed surface-brightness distribution of the background galaxy (*left panel*) and the residual image showing the remaining surface-brightness fluctuations to be studied in course of this paper (*right panel*).

Gaussian noise $\mathcal{N}(0, \sigma_n^2)$ with a variance σ_n^2 adapted to the flux value in a particular pixel.

However, due to noise correlations in the drizzled HST/WFC3/F390W images, discussed in more detail in Appendix A, the noise correction of the investigated residual surface-brightness fluctuations requires an even more extended approach

than just considering the noise-sigma map. In order to quantify the noise-correlation pattern induced in the analysed science image by the drizzling procedure and the CTI of the HST/WFC3/UVIS-CCDs, we select a sample of 20 empty-sky regions located in the proximity to the analysed lens and determine the average power spectrum in this sample. We account for the flux-dependent photon-

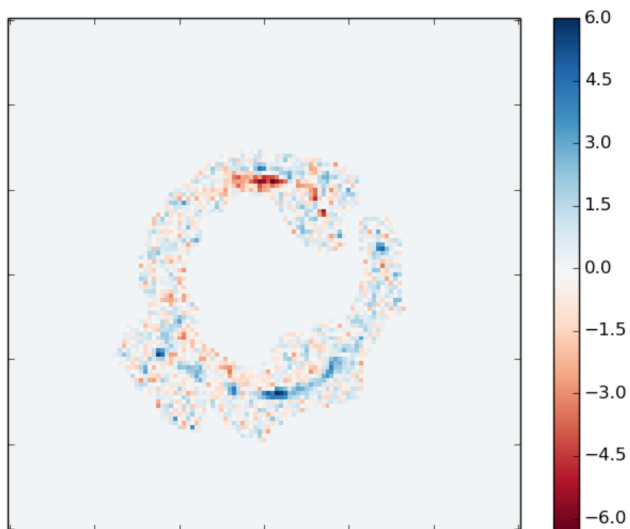


Figure 5. The signal-to-noise ratio of the residual surface-brightness fluctuations remaining in the lensed images of SDSS J0252+0039 after subtraction of the smooth-lens model with source-grid resolution $n = 3$ (casting back one pixel out of each contiguous 3×3 -pixel area).

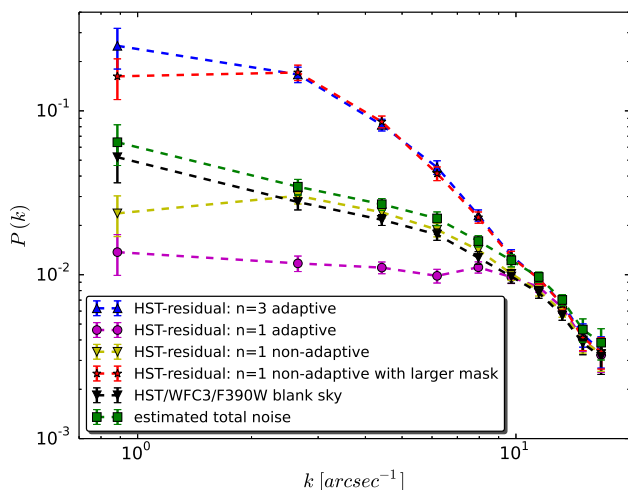


Figure 6. Power spectrum of the residual surface-brightness fluctuations in the lensed images of SDSS J0252+0039 after the smooth-lens modelling with the highest source-grid resolution ($n = 1$: constraining the source by casting back each pixel from the lens plane to the source plane using an adaptive (magenta line) or a non-adaptive (yellow line) source-grid regularisation) and with a lower source-grid resolution chosen for our analysis ($n = 3$: casting back only one pixel out of each contiguous 3×3 -pixel area; blue line), the sky-background noise-power spectrum estimated based on a sample of twenty selected empty-sky regions located in the proximity to the lens (black line) and the estimated total noise-power spectrum in the analysed science image including the flux-dependent photon-shot (Poisson) noise (green line). The red line shows the effect of using a larger mask combined with $n = 1$ and a non-adaptive source-grid regularisation.

shot (Poisson) noise present in the observed image of the lens by generating a modified version of these empty-sky regions: each of the 20 images is divided by the standard deviation of its flux values (in order to transform the data into the standard normal distribution) and multiplied by the noise-sigma map of the studied science image. These modified sky-background realisations account for both the realistic noise-correlation pattern of the drizzled HST/WFC3/F390W images and the specific spatially-varying flux-dependent photon-shot noise in the particular analysed science image. For consistency reasons, before calculating the noise-power spectra, the noise realisations are overlaid with the same mask as the one used to calculate the power spectrum of the residual surface-brightness fluctuations (described in Section 3.5). In what follows, the average power spectrum measured in this generated sample of modified empty-sky cutouts (Fig. 6) is used as our best estimate for the total noise-power spectrum in the analysed image of the studied lens system.

A comparison of the power spectrum of the residual surface-brightness fluctuations revealed in the lensed images of SDSS J0252+0039 with the estimated total noise-power spectrum shows that the measured surface-brightness fluctuations reach the noise level for the highest considered k -values (corresponding to scales below three pixels), which indicates that no surface-brightness anomalies have been detected on these scales (see Fig. 6). For this reason, in our further analysis we take into account only the five lowest k -bins, corresponding to scales above three pixels, for which the measured power spectrum of the residual surface-brightness fluctuations significantly exceeds the noise level. The further considered k -bins span the perturbation wave-number range between $k_{\min} = 0.88$ and $k_{\max} = 7.95 \text{ arcsec}^{-1}$ or, alternatively, the wavelength range between $\lambda_{\min} = 0.13$ and $\lambda_{\max} = 1.13 \text{ arcsec}$, corresponding to the physical scale range between $\lambda_{\min} = 0.52$ and $\lambda_{\max} = 4.65 \text{ kpc}$ at the redshift of the lens galaxy. Performing the analysis on scales above three pixels together with our choice of $n = 3$ in the smooth-lens modelling procedure allows us to neglect the effects of the PSF (with FWHM = 0.07 arcsec), the flux correlations in adjacent pixels due to drizzling and the possible residual errors in the source-light modelling.

Finally, we use this estimated total noise-power spectrum to perform the noise correction of the residual surface-brightness fluctuations measured within the chosen wave-number range assuming that the observational noise and the potential fluctuations $\delta\psi$, perturbing the smooth lensing potential, are independent stochastic processes. Consequently, we consider the corresponding power spectra to be additive, which allows us to subtract the estimated noise-power spectrum from the power spectrum of the total residual surface-brightness fluctuations measured in the observed HST image (see Fig. 7 for the result). The difference of these two power spectra constitutes our best estimate of the noise-corrected residual surface-brightness fluctuations and is treated in our further analysis as an upper limit to the power spectrum of the surface-brightness anomalies $P_{\delta I}(k)$ arising in the lensed images due to density fluctuations in the lensing-mass distribution.

3.7 Performance test with a realistic mock lens

Having uncovered the residual surface-brightness fluctuations $\delta I(\mathbf{x})$ (remaining in the lensed images after the lens-galaxy subtraction, the smooth-lens modelling and the noise correction) and quantified their statistical properties in terms of the azimuthally-averaged power spectrum $P_{\delta I}(k)$, we subsequently test the performance of our observational approach in recovering known surface-brightness

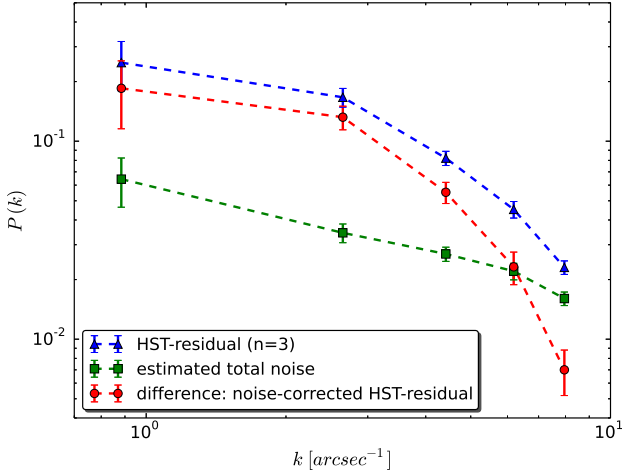


Figure 7. Noise correction: the power spectrum of the residual surface-brightness fluctuations in the lensed images of SDSS J0252+0039 after the smooth-lens modelling carried out casting back one pixel out of each contiguous 3×3 -pixel area ($n = 3$) (blue line), the estimated total noise-power spectrum (green line), and the difference between them - the upper limit to the surface-brightness anomalies due to mass structure in the lensing galaxy (red line).

anomalies from a mock HST-like image mimicking the real observations of the studied lens system.

The test mock-lens image is created based on the best-fitting smooth-lens model discussed in Section 3.4 – the reconstructed surface-brightness distribution $S(\mathbf{y})$ of the background source galaxy is lensed by the best-fitting smooth lensing potential $\psi_0(\mathbf{x})$ of the foreground lens galaxy perturbed with a superposed realisation of Gaussian potential fluctuations $\delta\psi_{\text{GRF}}(\mathbf{x})$. The GRF-potential perturbations $\delta\psi_{\text{GRF}}(\mathbf{x})$ are generated from the power-law power spectrum (see equation 13) with the variance $\sigma_{\delta\psi}^2 = 4 \times 10^{-4}$ and the power-law slope $\beta = 4$, chosen such that the power spectrum of the resulting surface-brightness anomalies in the lensed images resembles the residuals revealed in the real system. In order to account for observational effects, we convolve the lensed source emission with the Tiny-Tim PSF of the HST/WFC3/F390W optics and add a mock-noise realisation to the resulting image. For simplicity, this overlaid noise realisation is generated based solely on the noise-sigma map, described in Section 3.6, and does not incorporate the noise correlations found in the cutouts of empty sky from the observed HST/WFC3/F390W full-sky image (see Appendix A for more details). This simplifying assumption is justified by the low level of noise compared to the measured residual surface-brightness fluctuations. In a future analysis of further lens systems we will incorporate the noise correlation into the performance test.

For such a mock-lens system with a known potential-perturbation field $\delta\psi_{\text{GRF}}(\mathbf{x})$, full information is given about the power spectrum of the surface-brightness anomalies caused by $\delta\psi_{\text{GRF}}(\mathbf{x})$, the superposed noise realisation and the residual surface-brightness fluctuations due to the combination of these two effects (Fig. 8). This knowledge can be used to test the performance of the smooth-lens modelling code in recovering the known true power spectrum of surface-brightness anomalies induced by the perturbing potential fluctuations $\delta\psi_{\text{GRF}}(\mathbf{x})$ and fine-tune the choice of parameter values controlling the numerical algorithm. Here, we present the relevant results allowing us to determine the optimal number of

pixels n cast back from the lens plane to the source plane when using the previously chosen mask (depicted in Fig. 3) and the adaptive source regularisation.

With this aim, we use the methodology applied in Sections 3.4 and 3.5 to the observed data and perform the smooth-lens modelling of the mock lensed images for different values of $n = 1, 2, 3, 4$ to determine the resulting power spectra of the residual surface-brightness fluctuations. The smooth-lens modelling is carried out without re-optimising for the parameter values describing the smooth lensing potential. Hence, in this test we assume that the smooth lensing potential can be recovered accurately and focus on investigating the degeneracy between the perturbing mass structure in the lens and the small-scale surface-brightness fluctuations in the source galaxy itself. From Fig. 8 it can be seen that the power spectrum of the residual image from the smooth-lens modelling lies significantly below the noise level when each pixel is cast back from the lens plane to the source plane ($n = 1$; the highest resolution). As in the analysis of the real system, this overfitting can be explained by a partial absorption of the surface-brightness anomalies and the observational noise in the source structure.

While the underlying degeneracy between the potential perturbations in the lens and the intrinsic structure in the source is less problematic when trying to identify individual sub-haloes with masses above the detection limit as in Vegetti et al. (2014), this issue requires a more careful consideration in our power-spectrum analysis. As is apparent from Fig. 8, this degeneracy can be alleviated by lowering the source-grid resolution (choosing higher n -values), which leads to a better agreement between the reconstruction and the true power spectrum of the induced mock surface-brightness anomalies. A comparison of the residual power spectra corresponding to $n = 3$ and $n = 4$ (Fig. 8) suggests that convergence is reached for $n = 3$ and lowering the source resolution even further does not allow us to suppress this effect thoroughly (but would lead to a considerably less accurate source model) – the absorption of the potential fluctuations in the source structure still remains present on the smallest considered k -scales. We continue our analysis without excluding these small k -scales, which does not affect our final results significantly, as proved in a performed test.

All in all, based on the results of the above test with a realistic mock lens, we conclude that our approach allows us to recover the power spectrum of surface-brightness anomalies induced by the superposed known potential perturbations in the lens, when choosing the $n = 3$ resolution mode as the most suitable for our analysis. However, since the test is based on the previously reconstructed unlensed surface-brightness distribution of the source galaxy, which by construction can be easily modelled using the same smooth-lens modelling code, in what follows we still conservatively treat the recovered power spectrum as an upper limit to the effect caused solely by the potential fluctuations in the lens galaxy.

3.8 Mock perturbed lensed images

Assuming that the presented observational approach allows us to uncover and statistically quantify possible surface-brightness anomalies in the lensed images of the studied lens system (in terms of an upper limit), as demonstrated by the performance test in Section 3.7, in this section we create a set of realistic mock lensed images mimicking SDSS J0252+0039 for a systematic comparison with the observed data. To achieve this, we perturb the best-fitting smooth lensing potential of the studied lens system (see Table 1) with realisations of mock potential perturbations $\delta\psi_{\text{GRF}}(\mathbf{x})$ from the

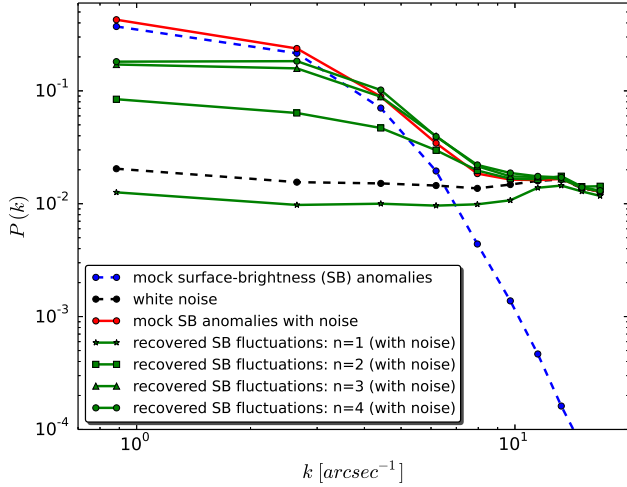


Figure 8. Performance test with a mock lens system mimicking SDSS J0252+0039. In order to test the performance of the smooth-modelling code in recovering possible surface-brightness anomalies present in the lensed images, we create a mock lens system by perturbing the best-fitting smooth lensing potential with GRF-potential fluctuations characterised by the power-law power spectrum $P_{\delta\psi}(k) \propto \sigma_{\delta\psi}^2 \times k^{-\beta}$ with variance $\sigma_{\delta\psi}^2 = 4 \times 10^{-4}$ and slope $\beta = 4$. The observational noise is mimicked by an overlaid white noise realisation (black line). The plot shows the one-dimensional azimuthally-averaged power spectrum of the true surface-brightness anomalies arising from the superposed potential perturbations $\delta\psi(\mathbf{x})$ (blue line), the power spectrum of these surface-brightness anomalies combined with the overlaid white noise realisation (true residual surface-brightness fluctuations, red line) and the power spectra of the residual surface-brightness fluctuations recovered from the mock perturbed lensed images in the smooth-modelling procedure with different source-grid resolutions (number of pixels cast back) $n = 1, 2, 3, 4$ without optimising for the parameter values of the smooth lensing potential (green lines from bottom to top).

associated GRF-power spectrum $P_{\delta\psi}(k; \sigma_{\delta\psi}^2, \beta)$ (defined in equation 13), repeat the lensing operation of the reconstructed unlensed background-source galaxy and examine the resulting gravitational signatures imprinted on the lensed images by the superposed Gaussian potential fluctuations for the entire range of $\sigma_{\delta\psi}^2$ and β .

The starting point of this procedure is the unperturbed smooth-lens model of the lensed emission $I_0(\mathbf{x})$, shown in the top panel of Fig. 9, comparable to the smooth-lens model reconstructed in Section 3.4 for our final choice of $n = 3$ and an adaptive regularisation. In order to simulate the observable surface-brightness anomalies induced in these smoothly lensed images as a result of the hypothetical GRF-potential perturbations $\delta\psi_{\text{GRF}}(\mathbf{x})$ in the lens, we generate pixelated realisations of such Gaussian fluctuations $\delta\psi_{\text{GRF}}(\mathbf{x})$ from the corresponding power-law power spectrum $P_{\delta\psi}(k; \sigma_{\delta\psi}^2, \beta)$ (equations 13 and 17) and superimpose them on the original best-fitting smooth lensing potential $\psi_0(\mathbf{x})$. Performing the lensing operation of the pixelated background-source galaxy $S(\mathbf{y})$ with such a perturbed lensing potential $\psi_0(\mathbf{x}) + \delta\psi_{\text{GRF}}(\mathbf{x})$ enables us to create the corresponding mock perturbed lensed images that can be subsequently compared to the observed data. Fig. 9 shows three examples of such mock perturbed lensed images mimicking SDSS J0252+0039, for different values of $\sigma_{\delta\psi}^2$ and β , together with the underlying realisations of the GRF-potential perturbations $\delta\psi_{\text{GRF}}(\mathbf{x})$ and the corresponding convergence-perturbation field $\delta\kappa_{\text{GRF}}(\mathbf{x})$, causing the visible surface-brightness anomalies in the lensed images. Based on

the performance test discussed in Section 3.7 (see Fig. 8), we can assume that, if the mock lensed images were actually observed, our methodology would allow us to successfully recover these surface-brightness anomalies present in the considered k -range.

Following the methodology applied to the observed lensed images in Sections 3.4 and 3.5, we subsequently subtract the unperturbed smoothly-lensed images from the generated mock perturbed lensed images of the background-source galaxy and quantify the resulting mock surface-brightness anomalies in terms of the one-dimensional azimuthally-averaged power spectrum. For consistency reasons, we calculate the power spectrum of the mock surface-brightness anomalies within the same mask and using the same set of ten bins for the azimuthal averaging as for the observed lensed images. Furthermore, in order to improve statistical properties of our results and reduce the sample variance, we perform our analysis based on a sample with ten different realisations of potential perturbations $\delta\psi_{\text{GRF}}(\mathbf{x})$ from each underlying GRF-power spectrum, uniquely specified by the choice of the variance $\sigma_{\delta\psi}^2$ and the power-law power-spectrum slope β . For each of these single realisations, we generate the resulting mock perturbed lensed images and determine the power spectrum of the induced mock surface-brightness anomalies. The sample average of these power spectra resulting from perturbing the lensing potential with a particular underlying GRF constitutes our best estimate for the statistical properties of the induced surface-brightness anomalies.

For a systematic investigation of the relation between the power spectrum of the hypothetical GRF-potential perturbations $P_{\delta\psi}(k)$ in the lens and the power spectrum of the resulting observable surface-brightness anomalies $P_{\delta I}(k)$ in the lensed images, we create a grid containing 100×100 different combinations of β and $\sigma_{\delta\psi}^2$. The test interval for the power-law slope β consists of 100 equidistant values in the interval $[3, 8]$, whereas the variance of the perturbing GRF fluctuations $\sigma_{\delta\psi}^2$ within the studied image is varied by obtaining 100 points evenly spaced in the logarithmic range $[10^{-6}, 10^{-1}]$. By repeating the above procedure for each point in this parameter space (referred to as a matter power-spectrum model $P_{\delta\psi}(\sigma_{\delta\psi}^2, \beta, k)$), we obtain a library containing 10,000 mock power spectra of observable surface-brightness anomalies that would be measured in the lensed images of SDSS J0252+0039 if the underlying hypothetical GRF-potential perturbations $\delta\psi_{\text{GRF}}(\mathbf{x})$ were characterised by a particular combination of values for β and $\sigma_{\delta\psi}^2$ (see the example of nine such mock power spectra overlaid on the real measurement in Fig. 10). In the following section, we compare these generated mock power spectra to our real measurement and determine the resulting exclusion probability for each considered matter power-spectrum model.

3.9 Probability of matter power-spectrum model exclusion

Given the library with power spectra of mock surface-brightness anomalies, created in the previous Section 3.8, and the power spectrum of residual surface-brightness fluctuations $P_{\delta I}(k)$ actually measured in the lensed images of the studied lens system, in this section we discuss our approach allowing us to assess whether a particular mock power spectrum is significantly different from the real measurement $P_{\delta I}(k)$ so that the underlying GRF matter-power spectrum can be excluded. For a specific combination of its two free parameters $\sigma_{\delta\psi}^2$ and β , we quantify this difference by calculating the exclusion probability of the corresponding power-spectrum model.

While deriving the exclusion probabilities, we take into account our upper-limit considerations from Section 2.1. Due to the

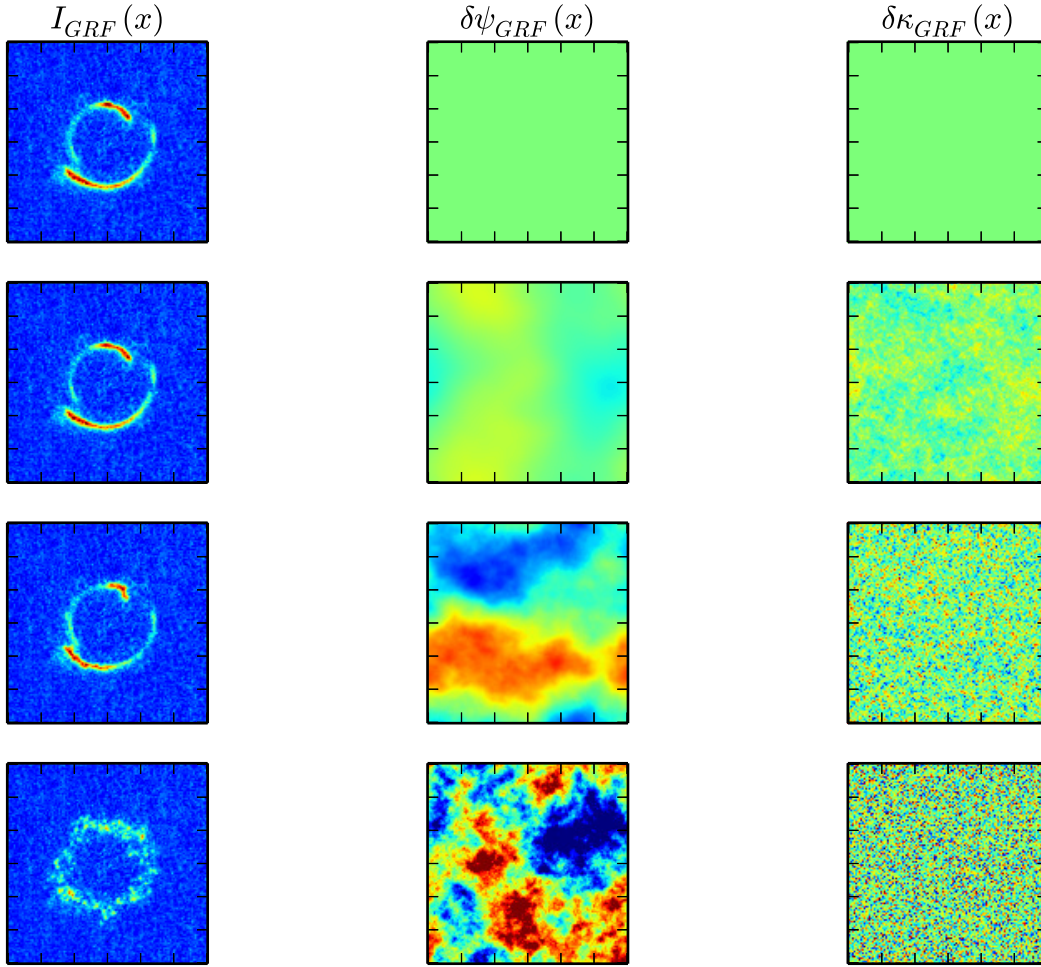


Figure 9. Observable simulated perturbations in the lensed emission of the background-source galaxy in SDSS J0252+0039 induced by mock realisations of GRF perturbations $\delta\psi_{\text{GRF}}(x)$ superposed on the best-fitting smoothly-varying lensing potential $\psi_0(x)$. *Left column:* the generated mock smooth lens mimicking the studied lens system (*upper panel*) and three examples of mock lensed images perturbed with GRF potential perturbations characterised by the power-law power spectrum with $\sigma_{\delta\psi}^2 = 2.154 \times 10^{-5}$ and $\beta = 5.5$, $\sigma_{\delta\psi}^2 = 2.783 \times 10^{-4}$ and $\beta = 4.25$ as well as with $\sigma_{\delta\psi}^2 = 10^{-3}$ and $\beta = 3$, respectively (*from top to bottom*). A realistic noise realisation (an empty-sky cutout corrected for photon-shot noise) is overlaid on the simulated lensed images for visualisation purposes. *Middle column:* the underlying realisations of the GRF-potential perturbations $\delta\psi_{\text{GRF}}(x)$. *Right column:* the corresponding realisations of the convergence perturbations $\delta\kappa_{\text{GRF}}(x) = \frac{1}{2} \nabla^2 \delta\psi_{\text{GRF}}(x)$.

regularisation and undersampling of the source plane in the smooth-lens modelling procedure, discussed in Section 3.4, the residual surface-brightness fluctuations revealed in the lensed images (after lens-galaxy subtraction, smooth-lens modelling and noise correction) might arise not only from density fluctuations in the lensing mass but also from not recovered structure in the original surface-brightness distribution of the background-source galaxy itself. Because of this possible degeneracy, we treat the measured residual surface-brightness fluctuations as an upper limit to the anomalies caused solely by GRF-potential perturbations $\delta\psi_{\text{GRF}}(x)$. Consequently, being conservative in excluding GRF power-spectrum models $P_{\delta\psi}(\sigma_{\delta\psi}^2, \beta, k)$ that are not in agreement with our measurement, we rule out a particular combination of $\sigma_{\delta\psi}^2$ and β only if the resulting mock power spectrum of surface-brightness anomalies $P_{\delta I}(k)$ from our library exceeds the observed power spectrum on all studied scales, in this case in all five analysed k -bins between $k_{\min} = 0.88$ and $k_{\max} = 7.95 \text{ arcsec}^{-1}$.

In order to compute the probability of exclusion for a given

combination of $\sigma_{\delta\psi}^2$ and β , we first calculate the probability that the value of the resulting mock power spectrum of surface-brightness anomalies in the lensed images $P_{\delta I}(k)$ is higher than the measured one for each of the considered k -bins separately:

$$P_{EX}(\sigma_{\delta\psi}^2, \beta, k) = \text{Prob}\left(P_{\delta I}^M(k) > P_{\delta I}^D(k) \mid \sigma_{\delta\psi}^2, \beta, P_{\delta\psi}(k) \propto \sigma_{\delta\psi}^2 \times k^{-\beta}\right) \quad (25)$$

with $P_{\delta I}^D(k)$ standing for the power-spectrum of the surface-brightness anomalies measured from data for a particular perturbation wavenumber k and $P_{\delta I}^M(k)$ representing the corresponding mock power-spectrum value for the particular choice of $\sigma_{\delta\psi}^2$ and β (power-spectrum model) from our library. In this calculation, we treat the power-spectrum value measured from data in each k -bin as the expected value of a Gaussian random variable with the standard deviation (corresponding to the error bars in Fig. 10) estimated based on the sample variance in our mock realisations of the total observational noise (discussed in Section 3.6).

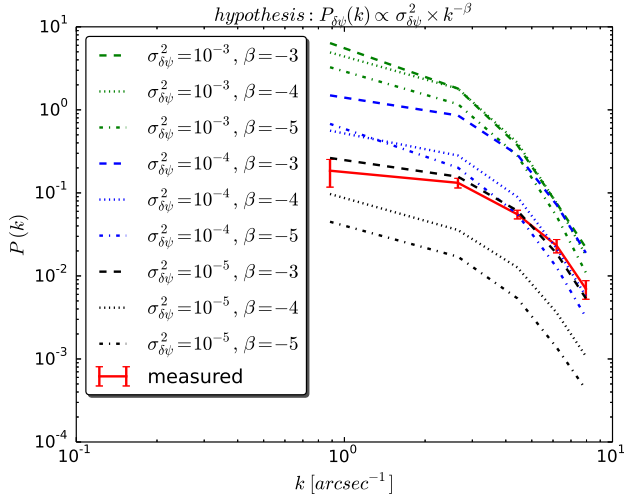


Figure 10. Mock power spectra of surface-brightness anomalies in the lensed images. The power spectrum of surface-brightness anomalies revealed in the lensed images of SDSS J0252+0039 (after the lens-galaxy subtraction, smooth-lens modelling and noise correction) (red line) is overlaid on a subset of the created library containing mock power spectra of surface-brightness anomalies arising from GRF perturbations to the best-fitting smooth lensing potential. Each considered combination of variance $\sigma_{\delta\psi}^2$ and slope β , uniquely characterising the power-law power spectrum $P_{\delta\psi}(k) \propto \sigma_{\delta\psi}^2 \times k^{-\beta}$ of the GRF-potential perturbations in the lens, is mapped onto the corresponding power spectrum of the arising surface-brightness anomalies in the lensed images. For simplicity, only 9 out of 10,000 computed mock power spectra are presented.

Assuming that our exclusion-probability estimates for different perturbation wavenumbers k are independent, the final exclusion probability for a particular matter power-spectrum model (combination of $\sigma_{\delta\psi}^2$ and β) is calculated as the product of the exclusion probabilities for all studied k -bins:

$$P_{\text{EX}}(\sigma_{\delta\psi}^2, \beta) = \prod_k P_{\text{EX}}(\sigma_{\delta\psi}^2, \beta, k). \quad (26)$$

The final probability of exclusion estimated based on our analysis of the pilot lens system SDSS J0252+0039 for the grid containing all considered matter power-spectrum models $P_{\delta\psi}(\sigma_{\delta\psi}^2, \beta, k)$ is presented in Fig. 11 and discussed in Section 4 as the main result of this work.

4 RESULTS

As outlined in the introduction, in this work we present a methodology that allows us to constrain the total matter-power spectrum on sub-galactic scales based on the power spectrum of surface-brightness anomalies measured in the lensed images of observed galaxy-galaxy strong gravitational lens systems. By applying this approach to our pilot lens system SDSS J0252+0039 from the SLACS Survey, in Section 3 we extracted the residual surface-brightness fluctuations from the analysed HST/WFC3/F390W-imaging of this system after performing the lens-galaxy subtraction (see Fig. 3), the smooth-lens modelling (see Fig. 4) and the noise correction (see Fig. 7). To quantify these residual fluctuations in a statistical way, we determined their one-dimensional azimuthally-averaged power spectrum $P_{\delta I}(k)$ (see Fig. 7), which

in this study is treated as an upper limit to the power spectrum of surface-brightness anomalies caused solely by the hypothetical GRF-potential perturbations $\delta\psi_{\text{GRF}}(\mathbf{x})$ in the lens galaxy. Next, in Section 3.8, we created a library containing power spectra $P_{\delta I}(k)$ of mock surface-brightness anomalies which would arise in the lensed images of the studied lens system as a result of the superposed GRF-potential perturbations $\delta\psi_{\text{GRF}}(\mathbf{x})$ with a specific choice of values for their variance $\sigma_{\delta\psi}^2$ and the power-law power-spectrum slope β , as illustrated in Fig. 10. Finally, in Section 3.9 we presented a way to compare the mock power spectra of surface-brightness anomalies from our library with the power spectrum $P_{\delta I}(k)$ actually measured in the observed image and calculated the probability of matter power-spectrum model exclusion (defined in equation 26) for each considered combination of $\sigma_{\delta\psi}^2$ and β .

In this section, we first present and discuss the inferred constraints on the statistical properties of the investigated hypothetical GRF-potential perturbations $\delta\psi_{\text{GRF}}(\mathbf{x})$ in the lens galaxy of SDSS J0252+0039 (Section 4.1), and trace them back to the underlying variance of the corresponding differential deflection angle (Section 4.2). Finally, we interpret these results in terms of the dimensionless convergence-power spectrum $\Delta_{\delta\kappa}^2(k)$ and the aperture mass on three specific spatial scales: 0.5, 1 and 3 kpc (Section 4.3), which enables a comparison with future theoretical predictions for different galaxy-formation and dark-matter models.

4.1 Upper-limit constraints on Gaussian potential fluctuations in SDSS J0252+0039

Our final constraints on the variance $\sigma_{\delta\psi}^2$ and the power-law power-spectrum slope β (as defined in equations 13-17) of the investigated hypothetical GRF-potential perturbations $\delta\psi_{\text{GRF}}(\mathbf{x})$ in the lens galaxy of our pilot lens system SDSS J0252+0039 are summarised in the exclusion plot presented in Fig. 11. Each point of the depicted two-dimensional grid corresponds to a particular matter power-spectrum model $P_{\delta\psi}(\sigma_{\delta\psi}^2, \beta, k)$, uniquely specified by the combination of values for $\sigma_{\delta\psi}^2$ and β . The presented grid contains a subset of 50×100 tested matter power-spectrum models with 50 different values evenly spaced in the logarithmic range $[10^{-5.0}, 10^{-2.5}]$ for $\sigma_{\delta\psi}^2$ and 100 values for β , equidistant in the interval $[3, 8]$. Colour-coded is the inferred probability of exclusion for the corresponding matter power-spectrum model $P_{\text{EX}}(\sigma_{\delta\psi}^2, \beta)$, i.e. the probability that the mock surface-brightness anomalies for the given model exceed the observed ones, as defined in equation (26). For all models lying above the superimposed (black) isoproability line, the inferred exclusion probability is larger than 99 per cent.

As evident from Fig. 11, our analysis of the pilot lens system allows us to rule out (with exclusion probability larger than 99 per cent) all matter power-spectrum models for which the variance $\sigma_{\delta\psi}^2$ of the GRF-potential fluctuations superimposed on the analysed image of SDSS J0252+0039 exceeds $\sim 10^{-2.5}$, corresponding to the standard-deviation threshold of $\sigma_{\delta\psi} \approx 0.06$. In accordance with our conservative approach, these excluded models lead to power spectra of surface-brightness anomalies $P_{\delta I}(k)$ that exceed the real measurement significantly on all studied scales. On the other hand, Fig. 11 shows that variance levels below $\sim 10^{-5}$ lead to surface-brightness anomalies that are significantly lower than what is measured for SDSS J0252+0039, independently of the slope β . However, due to the possible degeneracy between the additional gravitational effect of the investigated lensing mass-density

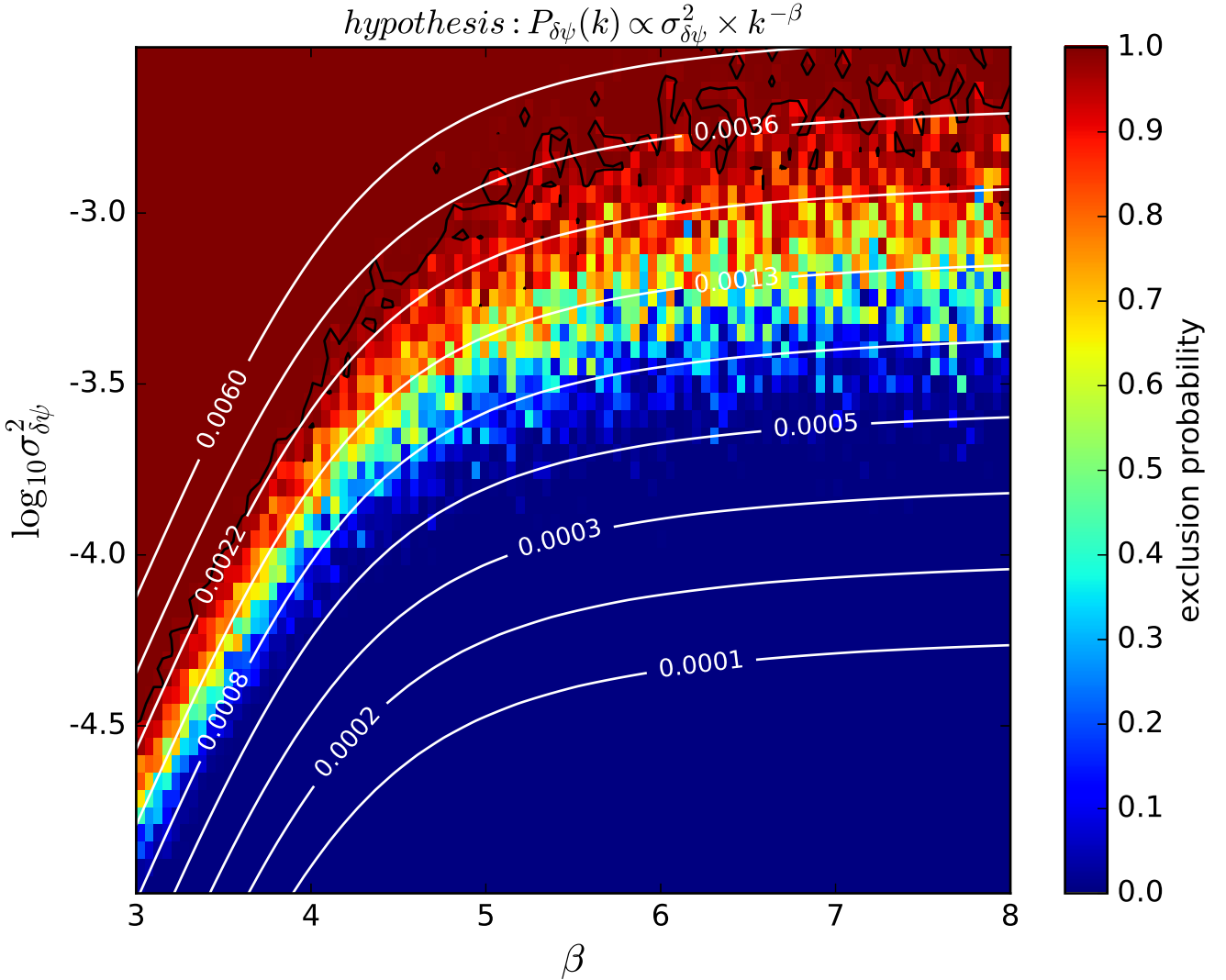


Figure 11. Exclusion plot for the power-spectrum parameters of the hypothetical GRF-potential perturbations $\delta\psi_{\text{GRF}}(x)$ in the lens galaxy SDSS J0252+0039. Each point of the exclusion plot corresponds to a particular power spectrum of the GRF-potential perturbations $P_{\delta\psi}(k) \propto \sigma_{\delta\psi}^2 \times k^{-\beta}$, uniquely specified by the combination of the variance $\sigma_{\delta\psi}^2$ and the power-law power-spectrum slope β (referred to as matter power-spectrum model). Colour-coded is the inferred probability of exclusion $P_{EX}(\sigma_{\delta\psi}^2, \beta)$ for each model with the 0.99-contour over-plotted in black. The white contour lines connect matter power-spectrum models corresponding to the same value of the total variance in the differential deflection $\sigma_{\delta\alpha}^2$ over the analysed field-of-view.

fluctuations and the structure in the lensed source itself, discussed in Section 2.1, we treat the measured residual surface-brightness fluctuations as an upper limit to the anomalies caused solely by GRF-potential perturbations $\delta\psi_{\text{GRF}}(x)$, and, thus, do not exclude matter power-spectrum models with surface-brightness anomalies below the measured level. Finally, in the range between $\sigma_{\delta\psi}^2 \sim 10^{-5}$ and $\sigma_{\delta\psi}^2 \sim 10^{-2.5}$ the exclusion probability depends on the chosen power-spectrum slope β , i.e. the exact distribution of the total variance between the different scales. For a given value of $\sigma_{\delta\psi}^2$, shallower slopes (lower absolute value of the power-law slope β), leading to more potential fluctuations on small scales (or large k -modes), are more likely to be excluded.

4.2 Upper-limit constraints on the differential deflection-angle field in SDSS J0252+0039

To explain the asymptotic shape of the exclusion plot in Fig. 11, we convert our original results for the power spectrum of GRF-potential perturbations $P_{\delta\psi}(k)$ into constraints on the power spectrum of the corresponding differential deflection-angle field $P_{\delta\alpha}(k)$. The differential deflection angle $\delta\alpha(x)$ contains full information about the additional lensing effect caused by the superposed realisation of the potential-perturbation field $\delta\psi(x)$ in each point of the lens plane and, thus, fully determines the resulting surface-brightness anomalies in the perturbed lensed images.

We use equation (19) to derive the power spectrum of the differential deflection-angle field $P_{\delta\alpha}(k, \sigma_{\delta\psi}^2, \beta)$ corresponding to the underlying power spectrum of the GRF-potential perturbations

$P_{\delta\psi}(k, \sigma_{\delta\psi}^2, \beta)$ for each point in our original exclusion-plot grid and, thus, for all considered combinations of $\sigma_{\delta\psi}^2$ and β . As can be seen in equation (19), the slope of this deflection-power spectrum decreases by two (in absolute terms, becoming shallower) with respect to the original slope of the potential-power spectrum. To obtain the associated total variance in the differential deflection angle $\sigma_{\delta\alpha}^2$ over the analysed field-of-view, we integrate the derived $P_{\delta\alpha}(k)$ over all pixels of the corresponding two-dimensional Fourier grid:

$$\sigma_{\delta\alpha}^2(\sigma_{\delta\psi}^2, \beta) = \int_{k_x} \int_{k_y} P_{\delta\alpha}(\sqrt{k_x^2 + k_y^2}, \sigma_{\delta\psi}^2, \beta) dk_x dk_y. \quad (27)$$

The results of this calculation are represented in Fig. 11 by the overlaid (white) isolines connecting matter power-spectrum models with the same values of the total variance in the differential deflection angle $\sigma_{\delta\alpha}^2$ over the analysed field-of-view.

As can be concluded from Fig. 11, the overlaid contours of the total variance in differential deflection angle $\sigma_{\delta\alpha}^2$ almost perfectly follow the overall shape of the exclusion plot. This strong correlation between the probability of matter power-spectrum model exclusion $P_{EX}(\sigma_{\delta\psi}^2, \beta)$ and $\sigma_{\delta\alpha}^2$ suggests that variance in the differential deflection angle over the analysed field-of-view $\sigma_{\delta\alpha}^2$, resulting from the underlying perturbing potential fluctuations $\delta\psi_{\text{GRF}}(\mathbf{x})$, is the crucial quantity determining the level of surface-brightness anomalies in the perturbed lensed images and, thus, the probability of the matter power-spectrum model exclusion. Thus, the exclusion probability is almost insensitive to the slope β of the $P_{\delta\alpha}(k)$, i.e. the distribution of the total variance in the deflection angle over the different length scales. Based on Fig. 11, we exclude (with 99 per cent probability) a matter power-spectrum model (specified by a particular combination of the original values for the variance $\sigma_{\delta\psi}^2$ and the slope β of the GRF potential perturbations $\delta\psi_{\text{GRF}}(\mathbf{x})$) if the corresponding total variance in the associated differential deflection field is larger than 6×10^{-3} , independently of the slope β .

All in all, we conclude that the probability of the matter power-spectrum model exclusion in our analysis is strongly determined by the total variance in the differential deflection angle, which leads to the exclusion of all models that exceed a certain threshold value of $\sigma_{\delta\alpha}^2$. This insight is valuable for our future analysis of further galaxy-scale lens systems which instead of potential perturbations $\delta\psi_{\text{GRF}}(\mathbf{x})$ might more efficiently focus on the effect of perturbations in the corresponding deflection-angle field $\delta\alpha_{\text{GRF}}(\mathbf{x})$. The inferred threshold value of the total variance in the differential deflection angle, however, might vary for different lens systems and depend on the chosen field-of-view.

For completeness, we additionally derive the corresponding upper-limit constraints on the associated dimensionless deflection-power spectrum $\Delta_{\delta\alpha}^2(k)$, defined in equation (22), for three different spatial scales 0.5, 1 and 3 kpc, and present them in Fig. 12. As evident from Fig. 12, we exclude the dimensionless deflection-power spectrum $\Delta_{\delta\alpha}^2(k)$ larger than 0.001 on all considered spatial scales (at the 99 per cent confidence level).

4.3 Upper-limit constraints on the surface-mass density fluctuations in SDSS J0252+0039

In order to make our results less dependent on the chosen field-of-view and allow for comparison with the more common approach to investigate density variations in terms of the convergence κ rather than the potential fluctuations, we now express and interpret our

constraints with respect to the dimensionless convergence-power spectrum $\Delta_{\delta\kappa}^2(k)$, defined in equation (21). With this aim, we determine $\Delta_{\delta\kappa}^2(k)$ corresponding to each matter power-spectrum model (combination of $\sigma_{\delta\psi}^2$ and β) considered in the exclusion plot (Fig. 11) for three different spatial scales: 0.5, 1 and 3 kpc. The smallest considered scale of 0.5 kpc corresponds to ~ 3 pixels - the smallest spatial scale taken into account in our analysis, as discussed in Section 3.7. The largest considered scale, on the other hand, is limited by the size of the analysed lensed images (gravitational arcs) in SDSS J0252+0039. Fig. 12 shows the resulting contour lines connecting matter power-spectrum models with the same value of the dimensionless convergence-power spectrum $\Delta_{\delta\kappa}^2$ inferred on a particular scale, overlaid on the original exclusion plot. Based on Fig. 12, we rule out matter power-spectrum models with the dimensionless convergence-power spectrum $\Delta_{\delta\kappa}^2$ larger than 1 on 0.5-kpc scale, larger than 0.1 on 1-kpc scale and larger than 0.01 on 3-kpc scale, at the 99 per cent confidence level.

These results can be additionally interpreted in terms of the standard deviation of the total convergence perturbation $\sigma_{\delta\kappa}(\lambda) \equiv \sqrt{\Delta_{\delta\kappa}^2(\lambda)}$ within the aperture diameter equal to the considered scale λ in an infinitely large sample of circular regions, randomly chosen in proximity of the Einstein radius. For the lensing-mass distribution of SDSS J0252+0039 we infer the following upper limits on this standard deviation: $\sigma_{\delta\kappa}(0.5 \text{ kpc}) < 1$ on 0.5-kpc scale, $\sigma_{\delta\kappa}(1 \text{ kpc}) < 0.3$ on 1-kpc scale and $\sigma_{\delta\kappa}(3 \text{ kpc}) < 0.1$ on 3-kpc scale. With the critical surface-mass density for SDSS J0252+0039 $\Sigma_{\text{cr}} \approx 4 \times 10^8 M_{\odot} \text{ kpc}^{-2}$, these constraints can be translated into the following upper-limits on the standard deviation $\sigma_{AM}(\lambda)$ in the aperture mass (total integrated mass of the corresponding convergence perturbation $\sigma_{\delta\kappa}(\lambda)$ within a cylinder of diameter λ projected onto the lens plane) in the inner region of the lens galaxy SDSS J0252+0039 due to the hypothetical Gaussian density fluctuations: $\sigma_{AM}(0.5 \text{ kpc}) < 0.8 \times 10^8 M_{\odot}$ inside the circular aperture of diameter $\lambda = 0.5 \text{ kpc}$, $\sigma_{AM}(1 \text{ kpc}) < 1 \times 10^8 M_{\odot}$ for the aperture diameter $\lambda = 1 \text{ kpc}$ and $\sigma_{AM}(3 \text{ kpc}) < 3 \times 10^8 M_{\odot}$ for $\lambda = 3 \text{ kpc}$ at the 99 per cent confidence level.

5 SUMMARY AND CONCLUSIONS

Various alternative dark-matter models and different galaxy-formation scenarios within the concordance Λ CDM model predict significantly different levels of mass structure on sub-galactic scales. Constraining the matter-power spectrum on 1-10 kpc-scales would make it possible to distinguish between these models. In this work, we have demonstrated a novel approach allowing us to observationally constrain the statistical nature of inhomogeneities (i.e. deviations from the smooth elliptical power-law density model with external shear) in the total projected mass distribution of (massive elliptical) lens galaxies from the measured power spectrum of the associated surface-brightness anomalies, observable in highly magnified galaxy-scale Einstein rings and gravitational arcs.

Following the theoretical framework developed by Chatterjee & Koopmans (2018), we model such inhomogeneities as Gaussian-Random-Field (GRF) potential perturbations, uniquely characterised by their variance $\sigma_{\delta\psi}^2$ and the slope β of the associated power-law power spectrum $P_{\delta\psi}(\sigma_{\delta\psi}^2, \beta, k)$. We consider a particular combination of these two parameters as a matter power-spectrum model and infer exclusion probabilities for a set of such models, given the imaging data of the studied lens system. Finally, to allow for comparison with theoretical predictions, we translate

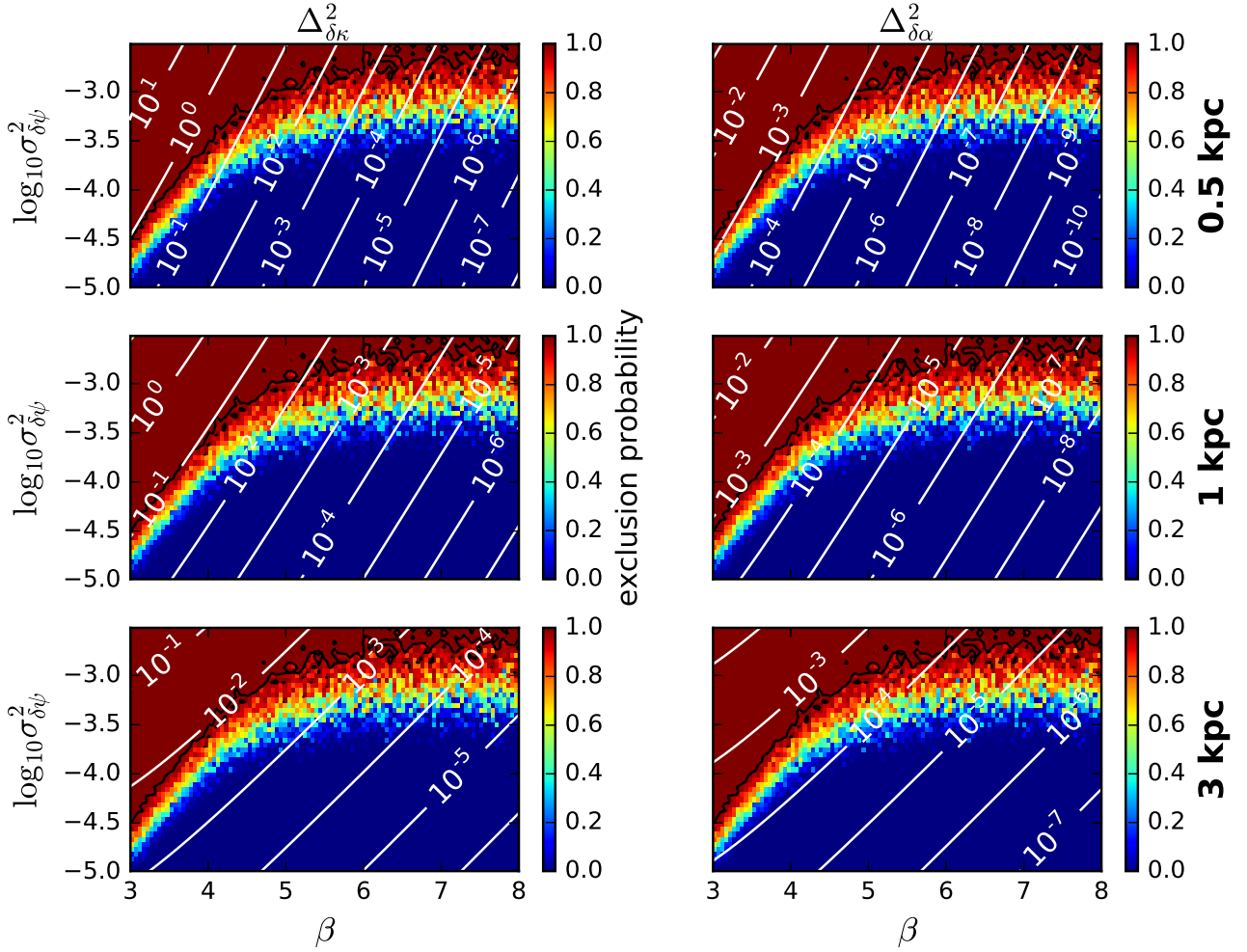


Figure 12. Upper-limit constraints on the dimensionless convergence-power spectrum $\Delta_{\delta\kappa}^2$ and the dimensionless differential deflection-power spectrum $\Delta_{\delta\alpha}^2$ in the lens galaxy SDSS J0252+0039 for three different sub-galactic scales. Each point of the underlying exclusion plot corresponds to a particular power spectrum of GRF-potential perturbations $P_{\delta\psi}(\sigma_{\delta\psi}^2, \beta, k)$ in the lens galaxy, uniquely specified by the combination of the variance $\sigma_{\delta\psi}^2$ and the power-law power-spectrum slope β (matter power-spectrum model). The white contour lines connect matter power-spectrum models corresponding to the same value of $\Delta_{\delta\kappa}^2$ (left panel) or $\Delta_{\delta\alpha}^2$ (right panel) on a particular scale. Overlaid in black is the 0.99-contour for the exclusion probability. Note that β represents the slope of the originally investigated power-spectrum of the potential perturbations $\delta\psi_{\text{GRF}}(\mathbf{x})$. The slopes of the associated power spectra of the convergence perturbations $\delta\kappa_{\text{GRF}}(\mathbf{x})$ and the deflection perturbations $\delta\alpha_{\text{GRF}}(\mathbf{x})$ decrease by 4 and 2, respectively (in terms of the absolute value).

these results into constraints on the corresponding dimensionless convergence-power spectrum $\Delta_{\delta\kappa}^2(k)$.

The pilot application of the presented methodology to the SLACS lens system SDSS J0252+0039 leads to the following conclusions:

(i) We rule out (with the exclusion probability of at least 99 per cent, depending on the slope of the associated power spectrum) GRF-potential perturbations $\delta\psi_{\text{GRF}}(\mathbf{x})$ with variance $\sigma_{\delta\psi}^2$ exceeding $\sim 10^{-2.5}$ in the analysed field-of-view (with the length $L \approx 20$ kpc on a side at the redshift of the lens galaxy), as apparent from Fig. 11.

(ii) We find that the crucial quantity determining the level of surface-brightness anomalies in the perturbed lensed images and, thus, the probability of the matter power-spectrum model exclusion, is the variance in the differential deflection angle $\sigma_{\delta\alpha}^2$ (in the analysed field-of-view) resulting from the underlying perturbing potential fluctuations $\delta\psi_{\text{GRF}}(\mathbf{x})$ (Fig. 11). Thus, the exclusion probability

seems to be almost insensitive to the slope β of the deflection-power spectrum $P_{\delta\alpha}(k)$, i.e. the distribution of the total variance in the deflection angle over the different length scales. Based on our analysis for SDSS J0252+0039, a matter power-spectrum model is excluded (with 99 per cent probability) if the variance of the resulting differential deflection field in the studied field-of-view $\sigma_{\delta\alpha}^2 > 6 \times 10^{-3}$, independently of the slope β . This insight is valuable for our future analysis of further galaxy-scale lens systems, that might be carried out by perturbing the deflection angle $\alpha(\mathbf{x})$ instead of the lensing potential $\psi(\mathbf{x})$. The threshold value itself, however, might vary for different lens systems and depend on the chosen field-of-view.

(iii) In order to make our results less dependent on the chosen field-of-view, we infer the corresponding constraints on the dimensionless convergence-power spectrum $\Delta_{\delta\kappa}^2(l)$ on three different sub-galactic scales and rule out matter power-spectrum models with $\Delta_{\delta\kappa}^2(0.5 \text{ kpc}) > 1$ on 0.5-kpc scale, $\Delta_{\delta\kappa}^2(1 \text{ kpc}) > 0.1$ on 1-kpc scale and $\Delta_{\delta\kappa}^2(3 \text{ kpc}) > 0.01$ on 3-kpc scale (at the 99 per cent confidence level).

(iv) The above constraints on the dimensionless convergence-power spectrum $\Delta_{\delta\kappa}^2(\lambda)$ can be interpreted in terms of the standard deviation of the total convergence perturbation $\sigma_{\delta\kappa}(\lambda) \equiv \sqrt{\Delta_{\delta\kappa}^2(\lambda)}$ in an infinitely large sample of circular regions with an aperture diameter equal to the considered scale λ , randomly chosen in proximity of the Einstein radius. For the lensing-mass distribution of SDSS J0252+0039 we infer the following upper-limit constraints on this standard deviation: $\sigma_{\delta\kappa}(0.5 \text{ kpc}) < 1$ on 0.5-kpc scale, $\sigma_{\delta\kappa}(1 \text{ kpc}) < 0.3$ on 1-kpc scale and $\sigma_{\delta\kappa}(3 \text{ kpc}) < 0.1$ on 3-kpc scale (at the 99 per cent confidence level).

(v) Alternatively, these constraints can be translated into the following upper limits on the standard deviation $\sigma_{AM}(\lambda)$ in the aperture mass (total integrated mass of the corresponding convergence perturbation $\sigma_{\delta\kappa}(\lambda)$ within a cylinder of diameter λ projected onto the lens plane) due to the hypothetical Gaussian density fluctuations in the inner region of the lens galaxy SDSS J0252+0039: $\sigma_{AM}(0.5 \text{ kpc}) < 0.8 \times 10^8 M_{\odot}$ inside the circular aperture of diameter $\lambda = 0.5 \text{ kpc}$, $\sigma_{AM}(1 \text{ kpc}) < 1 \times 10^8 M_{\odot}$ for the aperture diameter $\lambda = 1 \text{ kpc}$ and $\sigma_{AM}(3 \text{ kpc}) < 3 \times 10^8 M_{\odot}$ for $\lambda = 3 \text{ kpc}$ (at the 99 per cent confidence level).

To our knowledge, this is the first study that infers observational constraints on the clumpiness of the total matter distribution on the sub-galactic 1-10 kpc scales. In a follow-up paper, we will compare our findings with predictions from hydrodynamical simulations based on the Λ CDM and alternative dark-matter models. Here, we provide a preliminary simplified heuristic comparison with the Λ CDM predictions by only accounting for the predicted contribution from CDM substructure in the host halo of the lens galaxy and neglecting both other fluctuations in the total (baryonic and dark) mass distribution of the lens galaxy and the additional lensing effects due to possible line-of-sight haloes.

In particular, we estimate the upper limits on the dimensionless convergence-power spectrum $\Delta_{\text{CDM}}^2(\lambda)$ due to CDM substructure in the host halo of the investigated lens galaxy in an analytical way, for simplicity treating the sub-haloes as point masses. We apply the Poisson statistics to analytically predict the number of such sub-haloes from the assumed CDM substructure-mass function of the form $dN/dM \propto M^{-1.9}$ (Springel et al. 2008), neglecting the suppression of the substructure population due to baryonic processes discussed by Despali et al. (2017). In our calculation, we further very conservatively assume the total mass of the lens halo to consist of dark matter with the projected substructure mass fraction (i.e. fraction of the dark-matter locked in sub-haloes) of 0.005 in the proximity to the Einstein radius for the sub-halo mass range between 4×10^6 and $4 \times 10^9 M_{\odot}$ (Vegetti & Koopmans 2009b). Taking into consideration that the studied lens galaxy is well described by the Singular Isothermal Sphere model (as proved in Section 3.4) with the convergence $\kappa = 0.5$ in the proximity to the Einstein radius, we estimate the following upper limits on $\Delta_{\text{CDM}}^2(\lambda)$ in the dark-matter halo of SDSS J0252+0039: $\Delta_{\text{CDM}}^2(0.5 \text{ kpc}) < 10^{-3}$ on 0.5-kpc scale, $\Delta_{\text{CDM}}^2(1 \text{ kpc}) < 4 \times 10^{-4}$ on 1-kpc scale and $\Delta_{\text{CDM}}^2(3 \text{ kpc}) < 10^{-4}$ on 3-kpc scale. While such a point-mass approach is only an approximation, it provides a conservative upper-limit constraint on the contribution from CDM substructure to the total matter power-spectrum of the investigated lens galaxy.

A comparison of this estimation with our observational constraints on $\Delta_{\delta\kappa}^2$ for a flat convergence-power spectrum (corresponding to the slope $\beta = 4$ of the potential-power spectrum depicted in Fig. 12) leads to the conclusion that the the estimated effect of CDM substructure lies significantly below the inferred obser-

vational upper-limits on all considered scales. Accounting for the more realistic NFW-density profile of CDM substructure (Navarro et al. 1996), instead of the assumed point-mass model, would lead to an even lower estimate for the convergence-power spectrum due to CDM substructure. This preliminary conclusion does not change even if we consider that in reality the total number of haloes perturbing the lensed images of SDSS J0252+0039 might be a few times higher than just the estimated number of sub-haloes in the lens galaxy, due to the possible presence of unbound haloes along the total line-of-sight (Despali et al. 2017). We attribute the above discrepancy mainly to the fact that, unlike our preliminary Λ CDM-based predictions, the observational upper-limit constraints inferred in this work refer to the total (dark and baryonic) mass distribution projected along the line-of-sight, including the complex baryonic and dark matter structure of the lens galaxy (e.g. Gilman et al. 2017b; Hsueh et al. 2017a) and the possible line-of-sight haloes. Future research will, therefore, adequately compare these observational results with the total matter-power spectra (including the contributions from sub-haloes, line-of-sight haloes as well as other fluctuations in the baryonic and dark-matter distribution of the lens galaxy) obtained from hydrodynamical simulations.

As a further complication, the revealed strong degeneracy between the complex surface-brightness structure of the source on the one hand and the deviation of the real lens-mass distribution from the best-fitting smooth model on the other hand might lead to an enhanced level of the surface-brightness residuals, which in this paper is accounted for by inferring solely the upper limits on the level of the investigated density fluctuations in the lensing mass distribution. Further work is planned to investigate this degeneracy between the source and the potential in more detail.

Finally, the presented constraints are currently based on the analysis of a single lens system and can potentially be lowered by deriving analogous results for a larger sample of galaxy-galaxy strong gravitational lens systems. In our next paper, we will apply the above methodology to another SLACS lens system and narrow down the inferred observational upper limits for a future comparison with hydrodynamical simulations. Such comparison will eventually allow us to test both galaxy-formation scenarios within the Λ CDM model and alternative dark-matter models that could lead to matter-power spectra significantly exceeding the observational upper limits on the critical 1-10 kpc scales.

ACKNOWLEDGEMENTS

This study is based on observations made with the NASA/ESA *Hubble Space Telescope*, obtained from the data archive at the Space Telescope Science Institute. Support for this work was provided by a VICI grant (project number 614.001.206) from the Netherlands Organization for Scientific Research (NWO) and by a NASA grant (HST-GO-12898) from the Space Telescope Science Institute. STScI is operated by the Association of Universities for Research in Astronomy, Inc. under NASA contract NAS 5-26555.

REFERENCES

- Auger M. W., Treu T., Bolton A. S., Gavazzi R., Koopmans L. V. E., Marshall P. J., Bundy K., Moustakas L. A., 2009, *ApJ*, **705**, 1099
- Auger M. W., Treu T., Bolton A. S., Gavazzi R., Koopmans L. V. E., Marshall P. J., Moustakas L. A., Burles S., 2010, *ApJ*, **724**, 511
- Baggett S., Gossmeier C., Noeske K., 2015, Technical report, WFC3/UVIS Charge Transfer Efficiency 2009-2015

Barkana R., 1998, *ApJ*, 502, 531

Blandford R., Surpi G., Kundlíč T., 2001, in Brainerd T. G., Kochanek C. S., eds, *Astronomical Society of the Pacific Conference Series Vol. 237, Gravitational Lensing: Recent Progress and Future Go.* p. 65 ([arXiv:astro-ph/0001496](https://arxiv.org/abs/astro-ph/0001496))

Bode P., Ostriker J. P., Turok N., 2001, *ApJ*, 556, 93

Bolton A. S., Burles S., Koopmans L. V. E., Treu T., Moustakas L. A., 2006, *ApJ*, 638, 703

Bolton A. S., Burles S., Koopmans L. V. E., Treu T., Gavazzi R., Moustakas L. A., Wayth R., Schlegel D. J., 2008, *ApJ*, 682, 964

Bullock J. S., Boylan-Kolchin M., 2017, *ARA&A*, 55, 343

Bullock J. S., Kravtsov A. V., Weinberg D. H., 2000, *ApJ*, 539, 517

Bus S., 2012, bachelor thesis, Kapteyn Astronomical Institute

Casertano S., et al., 2000, *AJ*, 120, 2747

Chatterjee S., Koopmans L. V. E., 2018, *MNRAS*, 474, 1762

Dalal N., Kochanek C. S., 2002, *ApJ*, 572, 25

Despali G., Vegetti S., White S. D. M., Giocoli C., van den Bosch F. C., 2017, preprint, ([arXiv:1710.05029](https://arxiv.org/abs/1710.05029))

Diaz Rivero A., Cyr-Racine F.-Y., Dvorkin C., 2018, *Phys. Rev. D*, 97, 023001

Diemand J., Kuhlen M., Madau P., 2007, *ApJ*, 657, 262

Dooley G. A., Peter A. H. G., Carlin J. L., Frebel A., Bechtol K., Willman B., 2017, *MNRAS*, 472, 1060

Drlica-Wagner A., et al., 2015, *ApJ*, 813, 109

Gilman D., Birrer S., Treu T., Keeton C. R., 2017a, preprint, ([arXiv:1712.04945](https://arxiv.org/abs/1712.04945))

Gilman D., Agnello A., Treu T., Keeton C. R., Nierenberg A. M., 2017b, *MNRAS*, 467, 3970

Gonzaga S., Hack W., Fruchter A., Mack J., 2012, *The DrizzlePac Handbook*. STScI, Baltimore

Guo H., et al., 2016, *MNRAS*, 459, 3040

Hezaveh Y., Dalal N., Holder G., Kisner T., Kuhlen M., Perreault Levasseur L., 2016, *J. Cosmology Astropart. Phys.*, 11, 048

Hsueh J.-W., Fassnacht C. D., Vegetti S., McKean J. P., Spingola C., Auger M. W., Koopmans L. V. E., Lagattuta D. J., 2016, *MNRAS*, 463, L51

Hsueh J.-W., Despali G., Vegetti S., Xu D., Fassnacht C. D., Metcalf R. B., 2017a, preprint, ([arXiv:1707.07680](https://arxiv.org/abs/1707.07680))

Hsueh J.-W., et al., 2017b, *MNRAS*, 469, 3713

Kim S. Y., Peter A. H. G., Hargis J. R., 2017, preprint, ([arXiv:1711.06267](https://arxiv.org/abs/1711.06267))

Klypin A., Kravtsov A. V., Valenzuela O., Prada F., 1999, *ApJ*, 522, 82

Koopmans L. V. E., 2005, *MNRAS*, 363, 1136

Krist J., Hook R., Stoehr R., 2010, *Tiny Tim: Simulated Hubble Space Telescope PSFs*, Astrophysics Source Code Library ([ascl:1010.057](https://arxiv.org/abs/ascl:1010.057))

Lovell M. R., Frenk C. S., Eke V. R., Jenkins A., Gao L., Theuns T., 2014, *MNRAS*, 439, 300

Mao S., Schneider P., 1998, *MNRAS*, 295, 587

McConnachie A. W., 2012, *AJ*, 144, 4

Menci N., Fiore F., Lamastra A., 2012, *MNRAS*, 421, 2384

Metcalf R. B., Madau P., 2001, *ApJ*, 563, 9

Moore B., Ghigna S., Governato F., Lake G., Quinn T., Stadel J., Tozzi P., 1999, *ApJ*, 524, L19

Muller O., Pawlowski M. S., Jerjen H., Lelli F., 2018, *Science*, 359, 534

Navarro J. F., Frenk C. S., White S. D. M., 1996, *ApJ*, 462, 563

Nierenberg A. M., Treu T., Menci N., Lu Y., Wang W., 2013, *ApJ*, 772, 146

Nierenberg A. M., Treu T., Wright S. A., Fassnacht C. D., Auger M. W., 2014, *MNRAS*, 442, 2434

Nierenberg A. M., Treu T., Menci N., Lu Y., Torrey P., Vogelsberger M., 2016, *MNRAS*, 462, 4473

Peng C. Y., Ho L. C., Impey C. D., Rix H.-W., 2002, *AJ*, 124, 266

Planck Collaboration et al., 2016, *A&A*, 594, A1

Rau S., Vegetti S., White S. D. M., 2013, *MNRAS*, 430, 2232

Sawala T., et al., 2014, preprint, ([arXiv:1412.2748](https://arxiv.org/abs/1412.2748))

Schaye J., et al., 2015, *MNRAS*, 446, 521

Sérsic J. L., 1963, *Boletín de la Asociación Argentina de Astronomía La Plata Argentina*, 6, 41

Somerville R. S., 2002, *ApJ*, 572, L23

Springel V., et al., 2008, *MNRAS*, 391, 1685

Suyu S. H., Marshall P. J., Hobson M. P., Blandford R. D., 2006, *MNRAS*, 371, 983

Thoul A. A., Weinberg D. H., 1996, *ApJ*, 465, 608

Vegetti S., Koopmans L. V. E., 2009a, *MNRAS*, 392, 945

Vegetti S., Koopmans L. V. E., 2009b, *MNRAS*, 400, 1583

Vegetti S., Czoske O., Koopmans L. V. E., 2010a, *MNRAS*, 407, 225

Vegetti S., Koopmans L. V. E., Bolton A., Treu T., Gavazzi R., 2010b, *MNRAS*, 408, 1969

Vegetti S., Koopmans L. V. E., Bolton A., Treu T., Gavazzi R., 2010c, *MNRAS*, 408, 1969

Vegetti S., Lagattuta D. J., McKean J. P., Auger M. W., Fassnacht C. D., Koopmans L. V. E., 2012, *Nature*, 481, 341

Vegetti S., Koopmans L. V. E., Auger M. W., Treu T., Bolton A. S., 2014, *MNRAS*, 442, 2017

Vegetti S., Despali G., Lovell M. R., Enzi W., 2018, preprint, ([arXiv:1801.01505](https://arxiv.org/abs/1801.01505))

Viel M., Becker G. D., Bolton J. S., Haehnelt M. G., 2013, *Phys. Rev. D*, 88, 043502

Vogelsberger M., et al., 2014, *Nature*, 509, 177

APPENDIX A: NOISE-POWER SPECTRUM OF THE DRIZZLED HST/WFC3/F390W IMAGES

As discussed in Section 3.6, one of the crucial steps in our methodology is to account for the observational noise contributing to the measured residual surface-brightness fluctuations in the lensed images. Despite the fact that the pixels in our raw HST/WFC3/F390W-images can be considered to be independent, the observational noise in the drizzled images shows correlations caused by the drizzling procedure (see Casertano et al. (2000) for a more detailed explanation) as well as the charge-transfer inefficiency (CTI) in the HST/WFC3/UVIS-CCDs (see e.g. Baggett et al. 2015). The effect of this noise correlation is demonstrated in Fig. A1 showing a scale-dependent (one-dimensional azimuthally-averaged mean) power spectrum measured in an observed sample of 20 selected empty-sky regions located close to the studied lens system. For comparison, we additionally plot the flat power spectrum obtained for a mock sample containing 20 realisations of uncorrelated Gaussian noise process with the same standard deviation as in the observed empty-sky cutouts. Both samples consist of images with the same size as the analysed image of the studied lens system (121 by 121 pixels).

In order to investigate and possibly suppress the noise correlation in our HST/WFC3/F390W images of SDSS J0252+0039, we test the effect of different settings for the drizzling parameters *final scale* and *final pixfrac* when running the `ASTRODRIZZLE` task from the `DRIZZLEPAC` package (Gonzaga et al. 2012), in comparison to performing the drizzling procedure using default parameter values, as chosen for our analysis in this paper. By default, HST/WFC3/F390W images are drizzled to the original output pixel scale of 0.0396 arcsec/pixel (*final scale* = 0.0396 arcsec) without shrinking the input pixels (referred to as *drops* in the drizzling procedure) before mapping them onto the final output grid (*final pixfrac* = 1). As can be seen in Fig. A2, shrinking the output pixel size (lowering the value of the *final scale*) and the size of the drops (lowering the value of *final pixfrac*) when combining the raw dithered images does not significantly affect the measured power spectrum of the chosen empty-sky cutout in the five lowest *k*-bins taken into account in our analysis. Taking into account that choosing a lower final output-pixel scale while maintaining the same field of view in the studied science image would substantially increase the number of pixels and, thus, the computational effort for our methodology, we decide to proceed using the default configuration in the drizzling procedure.

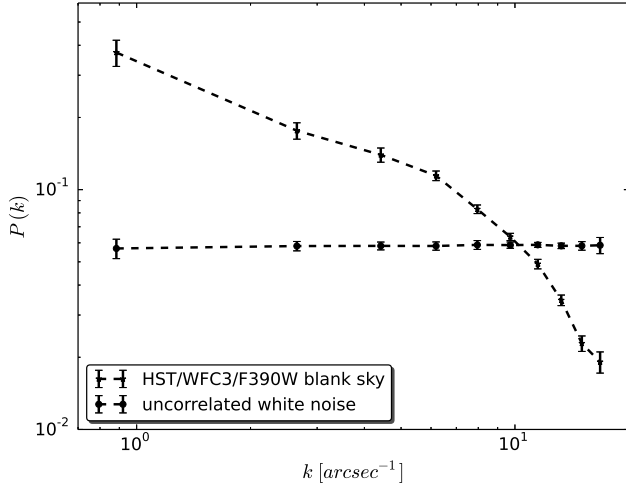


Figure A1. Noise correlation in the drizzled HST/WFC3/F390W images: the mean one-dimensional azimuthally-averaged power spectrum measured in a sample of twenty selected empty-sky regions located in proximity to SDSS J0252+0039 vs. the flat power spectrum measured in a sample of twenty mock realisations of uncorrelated Gaussian noise process with the same standard deviation as in the empty-sky cutouts.

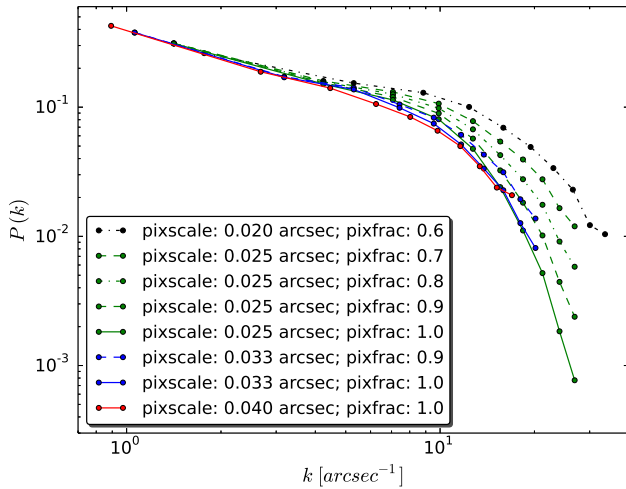


Figure A2. The effect of the drizzling parameters *pixscale* (final scale of the output pixels) and *final pixfrac* (size of the *drops*) on the one-dimensional azimuthally-averaged power spectrum of surface-brightness fluctuations measured in an empty-sky cutout close to SDSS J0252+0039 observed with HST/WFC3/F390W.

In addition to exploring different settings in the drizzling procedure, we test the possibility of performing the analysis using the drizzled CTI-corrected science image (obtained by drizzling CTI-corrected calibrated flc.fits files) instead of the original drizzled HST science image (obtained by drizzling the calibrated fit.fits files). The CTI-corrected calibrated files for WFC3/UVIS data became available from the MAST archive only after the beginning of our analysis. In order to test whether the CTI-correction would have a substantial effect on our results, we compare the power spectrum of the surface-brightness fluctuations measured in an empty-sky cutout close to SDSS J0252+0039 before and after the CTI-correction.

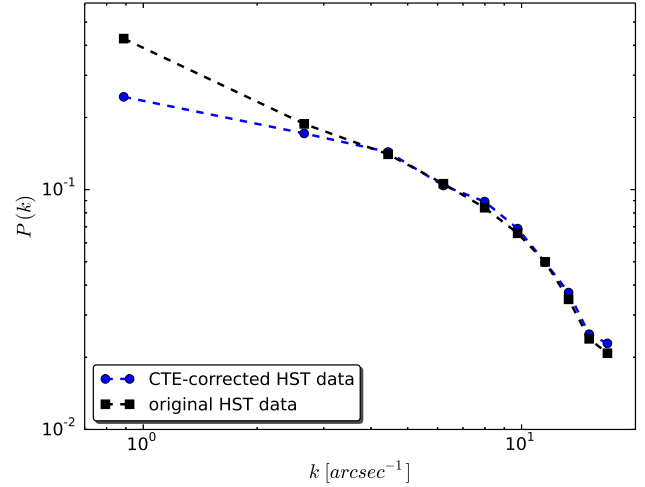


Figure A3. The effect of the charge-transfer efficiency (CTE) correction in the drizzling procedure on the measured power spectrum of surface-brightness fluctuations in HST/WFC3/F390W images: the one-dimensional azimuthally-averaged power spectrum of an empty-sky cutout close to SDSS J0252+0039 before vs. after CTE-correction (with the original pixel scale and the default value of *final pixfrac* = 1).

As demonstrated in Fig. A3, the CTI-correction does not affect the measured power spectrum on small scales but it leads to a significant reduction in noise correlation on the largest considered scale - the power for $\lambda = 1.13$ arcsec is roughly 40 per cent lower for the CTI-corrected drizzled science image. To investigate the impact of this largest considered scale (smallest considered k) on our final exclusion plot, we carry out a test run of our methodology for which we exclude this scale from the analysis. This test proves that the exclusion plot generated based on the reduced k -range (not presented in this paper) does not differ significantly from the original one. For this reason, we decide to proceed with our study using the original fit.fits files, not corrected for the CTI.

APPENDIX B: DUST ANALYSIS

Among all HST images available for SDSS J0252+0039 (U-, V-, I- and H-bands), the U-band photometry is most sensitive to the presence of dust. Thus, clumpy dust in the lens galaxy could potentially cause the small-scale variations in the surface brightness of the lensed images that, so far in this paper, have been interpreted as arising from density fluctuations in the lensing-mass distribution. In order to investigate this possible degeneracy, we compare co-aligned images of SDSS J0252+0039 in the U- and I-bands. For this comparison, the I-band image is drizzled to the reference frame and pixel size of the U-band image. The U-band image, on the other hand, is smoothed with a Gaussian profile to a larger blur (according to the Gaussian cascade smoothing) of the I-band image: the PSF of the F390W-filter is well described by a Gaussian profile with the FWHM 0.07 arcsec, whereas the PSF of the F814W filter has the FWHM 0.1 arcsec. Subsequently, both images are divided by the respective standard deviation of the photo-electron counts in the empty sky ($0.0012 \text{ e}^- \text{ sec}^{-1}$ for the smoothed U-band and $0.0045 \text{ e}^- \text{ sec}^{-1}$ for the I-band image drizzled to the pixel scale of the U-band) to obtain the signal-to-noise ratio for each pixel. Finally, to assess the effect of dust, we generate a ratio image between the I-

and the U-band and conclude that the variations present across the lensed images can be attributed to differences in the corresponding Point Spread Functions of the compared filters. An additional visual inspection of the colour-image in Fig. 1, based on observations in the UV (F390W), the visual (F814W) and the infrared bands (F160W), shows no indication for dust extinction either in the lens- or the source galaxy.

This paper has been typeset from a $\text{\TeX}/\text{\LaTeX}$ file prepared by the author.